Discovery and Resistance Mechanism of a Selective CDK12 Degrader

Baishan Jiang[1,2,8], **Yang Gao**[1,2,8], **Jianwei Che**[1,2,8], **Wenchao Lu**[1,2], **Ines H. Kaltheuner**[3], **Ruben Dries**[4,5], **Marian Kalocsay**[6], **Matthew J. Berberich**[6], **Jie Jiang**[1,2], **Inchul You**[1,2], **Nicholas Kwiatkowski**[1,2], **Kristin M. Riching**[7], **Danette L. Daniels**[7], **Peter K. Sorger**[6], **Matthias Geyer**[3], **Tinghu Zhang**[1,2,*], **Nathanael S. Gray**[1,2,*]

[1]Department of Cancer Biology, Dana–Farber Cancer Institute, Boston, Massachusetts, USA.

[2]Department of Biological Chemistry and Molecular Pharmacology, Harvard Medical School, Boston, Massachusetts, USA.

[3]Institute of Structural Biology, University of Bonn, Bonn, Germany.

[4]Department of Hematology and Oncology, Boston University, Boston, Massachusetts, USA.

[5]Department of Computational Medicine, Boston University, Boston, Massachusetts, USA.

[6]Laboratory of Systems Pharmacology, Harvard Medical School, Boston, Massachusetts, USA.

[7]Promega Corporation, Madison, Wisconsin, USA.

[8]These authors contributed equally: Baishan Jiang, Yang Gao and Jianwei Che.

Abstract

Cyclin-dependent kinase 12 (CDK12) is an emerging therapeutic target due to its role in regulating transcription of DNA damage response (DDR) genes. However, development of selective small molecules targeting CDK12 has been challenging due to the high degree of homology between kinase domains of CDK12 and other transcriptional CDKs, most notably CDK13. Here, we report the rational design and characterization of a CDK12 specific degrader, BSJ-4-116. BSJ-4-116 selectively degraded CDK12 as assessed through quantitative proteomics. Selective degradation of CDK12 resulted in premature cleavage and polyadenylation (PCPA) of DDR genes. Moreover, BSJ-4-116 exhibited potent antiproliferative effects, alone and in combination with the PARP inhibitor Olaparib, as well as when used as a single-agent against cell lines resistant to covalent CDK12 inhibitors. Two point-mutations in CDK12 were identified that confer resistance to BSJ-4-116 demonstrating a potential mechanism that tumor cells can use to evade bivalent degrader molecules.

Introduction

Cyclin-dependent kinases (CDKs) are serine/threonine protein kinases that play major roles in regulating many different aspects of mammalian cellular function, most notably cell cycle and transcription[1]. A majority of transcriptional CDKs[2–5] (CDK7, CDK9, CDK11, CDK12 and CDK13) catalyze multiple phosphorylation events on the carboxy-terminal domain (CTD) of RNA Pol II, a region of Pol II that consists of 52 heptapeptide (YSPTSPS) repeats. The pattern of phosphorylation of the CTD serves to regulate multiple aspects of transcription and post-transcriptional events. For example, CDK9-dependent phosphorylation of serine 2 in Pol II CTD repeat sequence is responsible for the transition from transcription initiation to productive elongation, and genetic depletion of CDK9 leads to a global downregulation of transcription[6]. On the other hand, in addition to regulating elongation, CDK12 phosphorylation of serine 2 sites on the 3′-end of genes was shown to be important for transcription termination and RNA processing[7]. The genetic loss of CDK12 results in a selective transcriptional defect for genes involved in cellular response to DNA damage, stress and heat shock[8–10]. CDK12 silencing, and the use of selective, covalent CDK12/13 inhibitor THZ531 (**1**) resulted in repression of DNA damage response (DDR)-associated genes, such as BRCA1 and ATR[11–13] (Extended Data Fig. 1a), by inducing usage of intronic polyadenylation, a process that produces truncated mRNA isoforms and results in aberrant protein production.

The genomic instability induced by CDK12 inactivation might provide an opportunity for cancer therapy. For example, ovarian and triple negative breast cancer cells with the lower expression of CDK12 are more sensitive to poly (ADP-ribose) polymerase inhibitor (PARPi) Olaparib and a combination treatment of Olaparib and Dinaciclib, a nonselective CDK12 inhibitor, synergistically suppressed tumor growth in PDX models[14,15]. In metastatic osteosarcoma, CDK12 inhibition sufficed to prevent lung colonization in ex vivo models with low MYC expression[16]. In addition, CDK12 inhibition exhibits synthetic lethality in other genetic or cellular contexts, e.g. MYC dependency[7,17], CHK1 inhibition[18] and EWS/FLI rearrangement[11,15]. This suggests that CDK12-directed targeted therapy, especially when combined with agents that inhibit DNA repair processes and that selective CDK12 inhibitors would be valuable both as research tools and as experimental therapeutics.

Currently available small molecule inhibitors cannot differentiate CDK12 and the closely related CDK13, as their ATP binding sites are essentially identical[19–23]. Although CDK12 and CDK13 are thought to be functionally redundant in some capacities such as their ability to phosphorylate serine 2 of Pol II[24], recent studies indicate that these kinases regulate transcription of distinct gene subsets [25,26]. Therefore, small molecules that selectively target CDK12 are needed to elucidate the biological functions of CDK12 and validate its therapeutic potential. Inspired by our recent success in developing selective degraders for closely related cell-cycle regulatory CDKs (CDK4 and CDK6), and a transcriptional CDK (CDK9)[27–29], we examined whether this strategy can be used to achieve selective CDK12 degradation. Here, we report the discovery of the first selective CDK12 degrader, BSJ-4-116 (**2**). We show that BSJ-4-116 downregulates the expression of DDR genes and exhibits anti-proliferative activity in cancer cells. We also demonstrate that CDK12 degradation alone or in combination with PARP inhibitors could be a therapeutic avenue for

targeting the intrinsic genomic instability in T-cell acute lymphoblastic leukemia (T-ALL) model. Importantly, although BSJ-4-116 overcomes resistance towards existing covalent inhibitors, we report that chronic exposure leads to acquired resistance to this compound through CDK12 mutation. These observations have important implications for degrader development, especially given that a proposed benefit of this class of degrader molecules is the ability to overcome resistance and minimize/abolish the rate at which drug resistance emerges[30–34].

Results

Design of a selective CDK12 degrader BSJ-4-116

The most common degrader molecules incorporate two molecular handles, one that recognizes and binds the protein of interest and one that binds an E3 ubiquitin ligase. The two handles are typically connected via a linker. Development of a successful degrader molecule usually requires optimization of the linker length, position and composition, selection of the appropriate target binder and E3 ligase and empirical screening for cell penetration, ternary complex formation and target degradation[35–37]. To rationally design a selective CDK12 degrader, we firstly analyzed the protein plasticity of CDK12/13 kinase domain in available crystal structures (PDB IDs of CDK12: 5ACB, 6CKX and 6B3E; PDB ID of CDK13: 5EFQ). We found that CDK12 has a higher conformational flexibility than CDK13 at the C-terminal tail, a CDK12/13 feature which is known to interact with ATP competitive inhibitors. We thus hypothesized that CDK12 has a higher tolerability than CDK13 with respect to the exit vector for linker attachment and degrader design. This suggested that CDK12-selective degrader might be achievable. Our starting point for CDK12-selective degrader design was the THZ531 scaffold, which is a dual CDK12/13 covalent inhibitor[19]. We dissected THZ531 into three fragments (**3**–**5**) that were profiled for CDK12 binding by induced-fit docking. As shown in Extended Data Fig. 1a, fragment 5 was suggested as the most efficient ligand (–0.41 ligand efficiency score). This predicted efficiency for fragment 5 was confirmed in biochemical assay (IC_{50} = 107 nM) (Extended Data Fig. 1b). Based on the predicted binding pose for fragment 5, we chose the piperidine moiety as the exit vector for installing the linker, followed by a ligand that has been extensively used to recruit cereblon (CRBN), an E3 ubiquitin ligase. A series of degrader molecules (**6**–**12**) were synthesized (Fig. 1a and Supplementary Table 1), and a primary screen by western-blotting led to identification of BSJ-4-23 as a potent CDK12 degrader (Extended Data Fig. 1c). A dose titration of BSJ-4-23 in Jurkat cells revealed significant degradation of CDK12 at 250nM while with the same concentration, CDK13 protein level was minimally affected (Fig. 1b).

We reasoned that the selectivity of BSJ-4-23 for CDK12 might be attributed to a failure to form a CRBN/BSJ-4-23/CDK13 ternary complex. To probe this possibility, we used computational modeling to generate the ternary complex structures of CDK12 and CDK13 with the degrader molecule and CRBN. BSJ-4-23 was found to fit tightly in the grooves between CDK12 and CRBN proteins and induces a complementary protein-protein interaction (PPI) (Extended Data Fig. 1d). By examining the putative PPI interface, we identified several possible key contributing factors to observed selective degradation of

CDK12. As shown in Fig. 1c, we noted that CDK12 Lys745 is located within a hydrogen bond distance from CRBN Cys394, while a corresponding residue in CDK13 (Arg723) disfavors the conformation with CRBN as indicated in the partial molecular surface overlapping between Arg723 of CDK13 and the nearby residues of CRBN. Importantly, as indicated by the residue surface of Arg723 (grey surface), CDK13 Met730 (yellow surface) was limiting the conformational space for Arg723 side chain through close contact and reinforcing the steric repulsion between CDK13 and CRBN. The model of the ternary complexes suggests that the (R)-3-amino piperidine position may represent a "privileged" exit vector position of CRBN-based degraders for CDK12 that might be transferable to other scaffolds. Therefore, we modified the ligand that was used for a promiscuous multi-kinase degrader molecule TL12–186 (**13**)[38] by replacing the 4-(piperazin-1-yl) aniline with (R)-3-amino piperidine to generate BSJ-4-116 and a negative control BSJ-4-116NC (**14**), in which the glutarimide nitrogen was methylated to block binding to CRBN[29] (Fig. 1d). As expected, BSJ-4-116 demonstrated a low nanomolar IC_{50} for inhibiting CDK12 enzymatic activity (Extended Data Fig. 1b) and exhibited potent CDK12 degradation in Jurkat cells in a dose- and time-dependent manner, while CDK13 protein level was minimally affected (Fig. 1e and Extended Data Fig. 1e). BSJ-4-116 also significantly suppressed the phosphorylation of Pol II Ser2 and Thr4, whereas p-Ser5 and p-Ser7 were not inhibited. Surprisingly, contrary to the report that CDK12 depletion by siRNA leads to Cyclin K degradation [39], BSJ-4-116-induced CDK12 degradation did not affect the Cyclin K protein level. As expected, BSJ-4-116NC and THZ531 had no effect on the levels of CDK13 and Cyclin K (Fig 1e). The CDK12 degradation induced by BSJ-4-116 was fully rescued by pretreatment with carfilzomib (a proteasome inhibitor), MLN4924 (a neddylation inhibitor that prevents CRBN activity by removing a critical post-translational modification needed for CRBN function), CDK12 covalent inhibitor THZ531 (competes for degrader binding on the target), and CRBN ligand Thalidomide (competes for degrader binding on the E3 ligase side) (Extended Data Fig. 1f). In addition, the rescue could also be realized through a genetic deletion of CRBN in Jurkat cells (Extended Data Fig. 1f). To determine the selectivity for kinase binding, we performed KINOMEscan profiling at concentration of 1 μM across a panel of 468 human kinases. BSJ-4-116 exhibited highly selective kinome profile, with a S-Score (10) value of 0.017 (Extended Data Fig. 1g and Supplementary Dataset 2). The selectivity for degradation was assessed by a proteome-wide profiling using Jurkat cells that were treated with 50 nM of BSJ-4-116 for 8h, then subjected to a multiplexed mass spectrometry (MS)-based proteomic analysis. These experiments detected CDK12 as the only kinase that was significantly degraded (by 4 folds) (Fig. 1f and Extended Data Fig. 1h). To understand the degrader selectivity for CDK12 over CDK13, we also utilized NanoBRET live cell ternary complex assays to monitor ternary complex formation. Robust ternary complex was induced between CDK12 and CRBN with BSJ-4-116, but not BSJ-4-116NC. And no appreciable ternary complex formation was observed between CDK13 with CRBN upon BSJ-4-116 treatment. As suggested by the computational model, a reduced ternary complex was observed between CRBN and either single mutant, or double mutant of K745L, L752M compared with wildtype CDK12. Interestingly, a single mutant of M730L or double mutant with R723K on CDK13 enhanced ternary complex formation with CRBN relative to wildtype CDK13 although R723K mutant alone did not show appreciable ternary complex with CRBN (Extended Data Fig. 1i). Taken together,

those findings demonstrated BSJ-4-116-induced CDK12 degradation is proteasome- and CRBN-dependent through efficient ternary complex formation, while sparing the closely related kinase CDK13.

BSJ-4-116 regulates DDR genes via PCPA

The regulation of DDR genes by CDK12 has been well documented using genetic knockdown and small molecule inhibitors such as THZ531[9,13]. To compare the pharmacological effects of our degrader molecule with that of an inhibitor, we performed 3' poly(A) sequencing in Jurkat cells exposed to BSJ-4-116, BSJ-4-116NC or THZ531 (Extended Data Fig. 2a). A concentration of 50 nM and 250 nM were chosen for BSJ-4-116 and THZ531, and 8 h exposure time-point to allow time for nearly complete CDK12 degradation (Extended Data Fig. 2b). As shown in Fig. 2a, the changes in gene expression due to treatment with THZ531 and BSJ-4-116 were highly correlated (Pearson r = 0.82, $R^2 = 0.67$) and resulted predominantly in decreased expression levels (Fig. 2a), with 7050 and 7123 downregulated transcripts (FDR <= 0.01), respectively (Fig. 2b). Overall, 115 upregulated transcripts and 6021 downregulated transcripts were shared between BSJ-4-116 and THZ531 treatments (Extended Data Fig. 2c). In contrast, direct pairwise comparison between BSJ-4-116 and THZ531 treated cells or between BSJ-4-116NC and DMSO control cells, showed only 211 genes (1.5% of total) and 1 gene differentially expressed, respectively. Gene set enrichment analysis (GSEA) demonstrated that genes involved in DDR pathway related processes were negatively enriched upon treatment with BSJ-4-116, with double strand break (DSB) repair as the most negatively enriched process (Extended Data Fig. 2d). For BSJ-4-116 there were two additional hits *tRNA Metabolic Process* and *Regulation of GTPase activity* (Extended Data Fig. 2e and Supplementary Dataset 3). This result is in line with the known enrichment for DDR genes with genetic perturbation of CDK12 or with THZ531 treatment (Extended Data Fig. 2f)[12,13,26]. Furthermore, the downregulation of DDR-related genes was evident at the mRNA level with 10 h treatment and protein level by 24 h, and, accordingly, we observed an increase in γ–H2AX, a marker of DNA damage, and apoptosis markers (Extended Data Fig. 2f).

Mechanistically, recent studies demonstrated that DDR genes under CDK12 regulation are enriched for specific genetic characteristics, such as increased gene length and low U1/ polyadenylation site (PAS) ratio, which makes them more susceptible to premature cleavage and polyadenylation (PCPA). Here, we noted that transcriptional downregulation observed with both BSJ-4-116 and THZ531 treatment was indeed associated with increased gene length (Fig. 2c). Next, to evaluate whether BSJ-4-116 treatment also causes PCPA, we focused on identifying poly(A) peaks associated with known upstream PAS motifs (Extended Data Fig. 2g). A metagene analysis of the distribution of poly(A) 3'-seq reads for all protein-coding genes across the genome revealed that BSJ-4-116 and THZ531, but not BSJ-4-116NC or DMSO, elicited significant loss of annotated terminal or 3' poly(A) sites (Fig. 2d and Extended Data Fig. 2h), and an increase in polyadenylated sites at the 5′ proximal ends of genes (Fig. 2e and Extended Data Fig. 2h). This observation could be attributed to a shift from the usage of canonical PAS within the 3' UTR, exonic polyadenylation sites to PAS within intronic regions at the 5' end (Extended Data Fig. 2i). Taken together, our data showed that a selective CDK12 small molecule degrader BSJ-04–

116 preferentially downregulated DDR genes by increasing PCPA, which resulted in early transcriptional termination, in line with previous results obtained using dual CDK12/13 inhibitor THZ531 (Extended Data Fig. 2j)[12,13]. This suggests that CDK12 alone is necessary and sufficient to suppress the use of cryptic intronic polyadenylation sites.

BSJ-4-116 synergizes with PARPi in T-ALL cells

To establish the growth rate inhibition profile of the degrader molecule, we conducted the experiments using BSJ-4-116, THZ531, and BSJ-04–116NC in wild-type (WT) T-ALL cell lines (Jurkat and MOLT4), as well as CRBN$^{-/-}$ cells, which were employed to assess CRBN-independent effects. The 3-day growth rate inhibition (GR) assays[40] were performed to evaluate sensitivity to CDK12 inhibition and degradation. BSJ-4-116 treatment resulted in comparable or lower GR$_{50}$s than THZ531 in WT TALL cells (Fig. 3a). Importantly, BSJ-4-116NC was 10-fold less potent than BSJ-4-116, indicating CDK12 degradation as the main mode of action. This was further supported by the observation that CRBN$^{-/-}$ cells displayed pronounced resistance to BSJ-4-116, while responding similarly to BSJ-4-116NC and THZ531 (Fig. 3a). Similar to THZ531, BSJ-4-116, but not BSJ-4-116NC, caused accumulation of G2/M cells (Extended Data Fig. 3a). Given that BSJ-4-116 was observed to downregulate transcription of genes involved in DDR pathways, we examined whether treatment with the degrader molecule sensitizes T-ALL cells to PARP inhibition. To examine the impact of CDK12 degradation and DDR inhibition, we combined BSJ-4-116 with a PARP inhibitor (PARPi), Olaparib, in WT Jurkat and MOLT4 cells. A strong synergistic interaction was observed as demonstrated by Bliss sum calculation (Fig. 3b). Such synergy was not observed in CRBN$^{-/-}$ cells (Extended Data Fig. 3b). Taken together, we demonstrate that the selective CDK12 degradation alone or in combination with a PARP inhibitor has strong growth inhibitory effects in T-ALL cell lines.

BSJ-4-116 overcomes CDK12 C1039F mutation

One of the potential advantages of degrader molecules is their ability to overcome drug resistance given their unique ternary complex formation and degradation-based mechanism of action. To assess the ability of BSJ-4-116 to inhibit the growth of drug resistant cell lines, we took advantage of neuroblastoma Kelly cells (KellyCDK12CF) that acquired CDK12^{C1039F} as resistant mutation during chronic exposure to E9, a covalent kinase inhibitor directed at Cys1039[20]. We treated parental and CDK12C1039F Kelly cells with BSJ-4-23, BSJ-4-116 or THZ531 for 6 h and 24 h, using DMSO treatment as a negative control. Addition of the degrader molecule led to the same level of CDK12 protein level decrease, regardless of the mutational status of the cell line (Fig. 3c). Moreover, antiproliferative activity of BSJ-4-116 and BSJ-4-23, but not THZ531, were also independent of the mutational status, and the degrader compounds exhibited improved GR$_{50}$s in Kelly CDK12^{C1039F} cells compared to parental cell line (Fig. 3d). Altogether, BSJ-4-116 represents a CDK12 chemical degrader with superior potency and selectivity than currently available small-molecule inhibitors.

CDK12 mutations lead to degrader resistance

Although capable of overcoming resistance to inhibitors as shown above and previously[30–32], degrader molecules may also lead to acquired resistance. However, the

mechanisms of degrader-acquired resistance are yet to be fully characterized. In addition to our interest in mechanisms behind acquired resistance to degraders, we have recently demonstrated that chronic selection of resistance can be used for target deconvolution and validation[20]. In this study, to ultimately validate CDK12 as the target for cell growth inhibition phenotype of BSJ-4-116 and further build on our understanding of the mechanisms of acquired resistance to bifunctional degraders, we exposed MOLT4 and Jurkat cells to increasing doses of BSJ-4-116 until they reproliferated at a normal rate under constant exposure of 0.5 μM of BSJ-4-116, approximately 10-fold of its GR_{50} in parental cells. As shown in Fig. 4a, in the presence of BSJ-4-116 or BSJ-4-23, the resistant cells retained CDK12 levels equivalent to those observed in parental cells treated with DMSO control. Resistant cells accordingly displayed a significant increase from 26 nM to 366 nM in GR_{50} (Fig. 4b and Extended Data Fig. 4a). To determine whether a loss of CDK12 engagement through mutation might have occurred, we first performed Sanger sequencing of the *CDK12* kinase domain in MOLT4 resistant cells and identified that CDK12 harbors a heterozygous point mutation I733V (Fig. 4c). To test the effect of this point mutation, we prepared recombinant I733V CDK12 and subjected it to *in vitro* kinase assays. These assays revealed that I733V conferred a slight gain-of kinase activity as well as loss of binding affinity with BSJ-4-23, BSJ-4-116 and THZ531 (Fig. 5a and 5b). Subsequently, a single-cell clone of Jurkat resistant cells was subjected to whole exome sequencing. Among the approximately nonsynonymous exonic 200 mutations excluding loss of function variants in resistant Jurkat cells that did not exist in parental cells (Supplementary Dataset 1), a single heterozygous point mutation G739S in CDK12 was identified and subsequently confirmed with sanger sequencing (Extended Data Fig. 4b). To our surprise, resistant cells remained equally sensitive to a recently developed CDK9 degrader THAL-SNS-032[27] (Extended Data Fig. 4c), further confirming that CRBN mediated proteasome machinery was still functional. Interestingly, G739 and I733 are located in the highly conserved Glycine-rich loop in the kinase domain that mediates ATP alignment and binding (Extended Data Fig. 4d)[41]. This prompted us to examine the binding capacity of a previously developed CDK7/12/13 covalent inhibitor THZ1, linked to biotin, via pulldown assays[19]. The lysate from either parental or resistant Jurkat cells was treated with Biotin-THZ1, enriched on streptavidin-agarose beads, and analyzed by western blotting to examine the protein levels. As shown in Fig. 5c, Biotin-THZ1 dose-dependently enriched CDK12 as well as cyclin K (commonly used as surrogate marker for CDK12 binding), both of which were entirely lost in resistant counterparts. In contrast, CDK7, as another covalent target of THZ1, displayed no differential enrichment in parental versus resistant cell lines. To examine the impact of these mutants on ternary complex formation, we performed NanoBRET live cell ternary complex assays in MOLT-4 cells transiently co-expressing HaloTag-CRBN and one of the following C-terminal NanoLuc fusions: CDK12, CDK12 (I733V) or CDK12 (G739S) to monitor the CRBN engagement in MOLT-4 cells. The fold increase in NanoBRET signal relative to a DMSO control was plotted after 3h-treatment with the indicated compounds with n=6 technical replicates. Robust ternary complex was induced between CDK12 and CRBN with BSJ-4-116, but not with BSJ-4-116-NC. No appreciable ternary complex formation was observed between CDK12 resistant mutants with CRBN, indicating that those evolving mutations can prevent ternary complex formation at molecular level which is needed for degradation by our CDK12 degraders (Fig. 5d). This phenomenon strongly

suggests the loss of direct degrader binding due to G-loop mutations as a mechanism for acquired resistance.

Discussion

CDK12 and its close homologue CDK13 are transcriptional CDKs, and individual genetic deletion of each led to downregulation of distinct subsets of genes[13,26]. DDR genes are preferentially sensitive to CDK12 deletion, which opens up a therapeutic potential for CDK12 inhibitors as treatments for cancers that harbor a proficient DNA damage repair function, such as those overexpressing BRAC1/2. However, development of pharmacological agents that are selective for CDK12 over CDK13 has not been achieved[19,22,23]. Degrader molecules present a novel pharmacological modality of chemical protein knockdown that has been shown to exhibit improved selectivity relative to parental inhibitors[27,38]. To discover a selective CDK12 degrader, we employed computational modeling and ligand efficiency calculations[42] as criteria for guiding degrader design, resulting in identification of fragment 5 as a privileged scaffold for selective CDK12 degradation. The computational analysis of the potential ternary complex between CDK12 and CRBN unveiled several features of CDK12 that we exploited to achieve selectivity over CDK13. As we show, fragment 5 takes advantage of the differences between the residues that are responsible for stabilizing PPI interactions, and the differences between intrinsic conformational flexibility between CDK12 and CDK13. Our modeling of fragment 5, a novel CDK12 binder derived from THZ531, and BSJ-4-23, a selective CDK12 degrader, identified the importance of the exit vector (R)-3-amino-piperidine in BSJ-4-23. Thus, guided by this finding, we were able to rationally design a highly potent and selective CDK12 degrader BSJ-4-116 by replacing the exit vector of TL12–86 with (R)-3-amino-piperidine. Using a range of *in vitro* and cell-based experiments, we validated BSJ-4-116 as the first CDK12 selective compound. Using BSJ-4-116 as a tool compound, we unambiguously validated the role of CDK12 in transcriptional regulation. For example, BSJ-4-116 downregulated DDR genes through a premature termination of transcription, primarily through increasing PCPA. The results we report here, together with recently published studies[12,13], strongly support the view that CDK12 activity is necessary and sufficient to suppress the use of cryptic intronic polyadenylation sites. Although, other reported redundant function of CDK12 and CDK13[24, 43], different cellular content might play a role for their functions, and our selective compounds could be helpful to delineate the functions in more detail.

In terms of potential application of CDK12 selective degraders as a therapeutic strategy, the results we obtained here using T-ALL cell lines suggest that CDK12 degraders alone or in combination with PARP inhibitors may offer a therapeutically relevant opportunity. Importantly, CDK12 degraders may be especially relevant to overcome the drug resistant CDK12 phenotypes characterized by an acquired C1039F mutation[13,20]. Having said that, similar to what has been seen for many other therapies, and especially small molecule-based inhibitors, prolonged (chronic) dosing with degraders may also result in acquired resistance phenotypes. Thus far, few reported cases that examined this possibility suggested that cells acquire resistance to degrader molecules by changing the composition of the E3 ligase complexes to exclude the E3 subunit that is essential for degrader binding, such as CRBN[44].

Here, we report another mechanism for acquired resistance that involves emergence of the mutations on the target protein. More specifically, we document that chronic exposure of MOLT4 and Jurkat cells to BSJ-4-116 led to the development of resistance to CDK12 degradation via point mutations on CDK12. We identified that two specific mutations on CDK12's G-loop, I733V and G739S, give rise to the observed resistance. Interestingly, we observe that I733V mutation both reduces BSJ-4-116 binding and enhances CDK12 kinase activity which together reduce the efficacy of the compound. In addition, cellular target engagement assays suggest that both mutants reduced not only CDK12 binding affinity for the degrader molecule but affinity for the covalent inhibitor THZ1 as well, while retaining an intact CRBN complex. Thus, to our knowledge, BSJ-4-116 represents the first example of resistance to a bivalent degrader molecule that is a consequence of an acquired point mutation in the target protein.

Online Methods

Chemistry.

Chemical synthesis and characterization are provided as a supplementary Note.

Molecular Docking.

Fragment docking.—Fragments were docked into CDK12 co-crystal structure (PDB ID: 5ACB) ATP binding pocket using induced-fit protocol from Schrodinger suite (version 2019 release 4). Standard protein preparation protocol was carried out prior to docking. Hinge hydrogen bonds with MET816 backbone were used as constraint to ensure the proper binding mode. Default values were adopted for other parameters. Ligand efficiency is defined as the following,

$$LE = GlideScore/(number\ of\ heavy\ atoms)$$

CRBN-CDK12 complex model prediction.—Protein-protein docking by Rosetta (v3.9) was used to generate ternary complex models of CDK12 and CRBN. The cocrystal structure of CRBN with lenalidomide (PDB ID: 4TZ4) and fragment 5 in CDK12 (PDB ID: 5ACB) were prepared for docking using protein preparation protocol in Schrodinger suite, and then followed by standard Rosetta protein-protein docking procedure. Flat bottom harmonic constraint was applied to amine nitrogen off the benzene ring and the piperidine N in fragment 5 for biasing the conformations within the range of practical degrader synthesis and reasonable molecular weight. The parameters were $x0 = 9$, $sd = 1$, $and\ tol = 7$ (https://www.rosettacommons.org/docs/latest/rosetta_basics/file_types/constraint-file). This constraint imposed no bias if the distance between the two nitrogen atoms were between 2 and 16 angstroms, and harmonic energy was added if the distance was outside the range. The range covered both close contact and reasonable linker length for forming ternary complexes. The sampling parameters for docking were "-ex1 -ex2aro -dock_pert 3 8" with constraint specified. 15000 CRBN CDK12 complex structures were generated, and 1500 top conformations were chosen for further analysis based on interface scores and satisfactory of the distance constraint. The top conformations were clustered by RMSD of CDK12 backbone heavy atoms as a measure of conformational diversity. 80 clusters were generated

using Schrodinger conformational clustering tool. The top conformation based on interface score was chosen as the ternary complex model with $I\_sc = -26.18$. The structure belonged to a cluster with 16 members and multiple of them ranked in the top scoring complexes (4 out 10).

Docking of degrader BSJ-4-23.—BSJ-4-23 was docked into predicted CRBN and CDK12 complex model using MOE (release 2019) template docking protocol. The glutarimide in CRBN binding pocket and amino pyrimidine in the CDK12 binding site were chosen as the templates. Default values were used for docking parameters and proteins were kept rigid during docking calculation. The top scored pose was further refined by protein-ligand complex refinement protocol in Schrodinger suite.

Cell culture.

Human T-cell acute lymphoblastic leukemia cell lines Jurkat and MOLT4 were obtained from ATCC. The cells were tested for mycoplasma routinely using MycoAlert mycoplasma detection kit (Lonza, LT07–318). All cell lines used in this study were maintained in RPMI 1640 medium (Cat#11875119; Thermo Fisher Scientific) supplemented with 10% FBS (Gibco) at 37 °C in a humidified chamber in the presence of 5% CO_2.

Western Blotting.

The cells were collected by trypsinization and washed with PBS buffer. Cell lysates were prepared by using NP40 lysis buffer (Invitrogen) supplemented with Complete protease inhibitor cocktail (Roche), PhosSTOP phosphatase inhibitor cocktail (Roche) and PMSF (1 mM). The lysates were cleared by centrifugation and resolved using Bolt™ 4–12% Bis-Tris plus gels and western blotted to detect proteins of interest. Antibodies used against various proteins were as follows: CDK12 (1:1000, Cell Signaling Technologies #11973), CDK13 (1:2000, Bethyl Laboratories #A301–458A), BRCA1 (1:1000, Cell Signaling Technologies #9010), BRCA2 (1:1000, Cell Signaling Technologies #10741), cleaved PARP (1:1000, Cell Signaling Technologies #5625), cleaved caspase 3 (1:1000, Cell Signaling Technologies #9661), α-tubulin (1:4000, Cell Signaling Technologies #3873), GAPDH (1:4000, Cell Signaling Technologies #2118), RAD51 (1:1000, Santa Cruz Biotechnologies #sc-8349), Anti-phospho-RNAPII Antibody (Ser2) (1:1000, Sigma-Aldrich #04–1571-I), Anti-phospho-RNAPII Antibody (Thr4) (1:1000, Sigma-Aldrich #MABE348), Anti-phospho-RNAPII Antibody (Ser5) (1:1000, Sigma-Aldrich #04–1572-I), Anti-phospho-RNAPII Antibody (Ser7) (1:1000, Sigma-Aldrich #04–1570-I), RNAPII (1:1000, Cell Signaling Technologies #14958). Antibodies were used according to the manufacturers' instructions. For western blot visualization, Odyssey Clx (Li-cor) was utilized.

Proteomics.

Methods described below were based on a reported protocol[45]. Cells were rinsed once with 1x sterile PBS and stored at −80°C. Cells were lysed by addition of SDS lysis buffer (2% SDS, 150 mM NaCl, 50 mM Tris, pH 8.7) containing protease and phosphatase inhibitors (Halt™ Protease and Phosphatase Inhibitor Single-Use Cocktail, EDTA Free, ThermoFisher, Catalog Number 78441). Lysate was then pipetted onto Qiashredder filters (Qiagen, ref.

79656) and centrifuged at max speed for 2 minutes, room temperature. Filtrate was collected and placed into microfuge tube.

Disulfide reduction was performed by adding dithiothreitol (DTT) to a final concentration of 5 mM and heating to 37°C for 1 hour, followed by alkylation with iodoacetamide at a final concentration of 15 mM and incubation at room temperature in the dark for 30 minutes and quenching with 50 mM freshly prepared DTT. Protein concentration was determined using a Micro BCA™ Protein Assay Kit (ThermoFisher, Catalog Number 23235) following the manufacturer's protocol. For each sample, an aliquot corresponding to 150 μg of total protein was withdrawn. Detergent was removed by methanol/chloroform protein precipitation as described previously[46]. Precipitates were solubilized in freshly prepared 8M urea in 200 mM EPPS, pH 8.5 and 60 μg of solubilized total protein from each sample was then used for TMT labelling. Following a 10 min incubation at 37°C, the urea concentration was diluted with 200 mM EPPS to 2M final concentration, 2% acetonitrile (v/v) was added and digestion was performed by overnight incubation at room temperature in the presence of Lys-C protease (Wako, Catalog Number 129–02541) at an enzyme-to-substrate ratio of 1:75. Following further dilution of the sample with 200 mM EPPS to a final urea concentration of 0.8 M in the presence of 2% acetonitrile (v/v), digestion was performed by incubation at 37°C for 6 hours with trypsin (Promega, Catalog Number V5113) at an enzyme to substrate ratio of 1:75.

Digest Check.—The missed cleavage rate was determined by LC-MS/MS. 1 μg of total protein was withdrawn from each sample and combined into a single sample. Only samples with a missed cleavage rate <10% were processed further.

TMT Labelling, Ratio Check and HPLC Fractionation.—Equal amounts of protein were removed from each sample and labelled using a TMT11plex Mass Tag Labelling Kit (ThermoFisher, Catalog Number A34808). TMT labelling efficiency and ratio checks were measured by LC-MS3 analysis of a combined 11-plex sample after combining equal volumes (about 1 μg) from each sample. Equal amounts of labelled peptide from each sample (as judged from ratio check data) were then combined for subsequent analysis.

Quenching of TMT labelling reactions was performed by adding hydroxylamine to a final concentration of 0.5% (v/v) and incubating samples for 10 minutes at room temperature. Formic acid (FA) was added to a final volume of 2% (v/v) to lower the pH below 3.0 and samples were combined and de-salted using a SepPak tC18 Vac RC Cartridge (50 mg, Waters, Catalog Number WAT054960). HPLC fractionation was performed using an Agilent 1200 Series instrument with a flow rate of 600 μl/minute over a period of 75 minutes. Peptides were collected in a 96-well plate over a 65 min-gradient of 13–44 %B with Buffer A comprising 5% acetonitrile, 10 mM ammonium bicarbonate, pH 8 and Buffer B comprising 90% acetonitrile,10 mM ammonium bicarbonate, pH 8. Fractions were then pooled into 24 samples, followed by sample clean-up using the Stage Tip protocol. This protocol uses C18 Empore™ Extraction Disks (Fisher Scientific, Catalog Number 14–386-2). The matrix was primed with methanol and equilibrated with 70% acetonitrile, 1% FA followed by washing twice with 1% FA, loading the sample in 1% FA, followed once

again by two 1% FA washes, and finally peptide elution using 70% acetonitrile, 1% FA. Samples were dried before resuspension in MS Loading Buffer (3% acetonitrile, 5% FA).

LC-MS.—Peptides were injected onto a 30 cm, 100 μm (internal diameter) column and separated using an EASY-nLC 1200 HPLC (ThermoFisher, Catalog Number LC120). The flow rate was 450 nl/min with a gradient of 6–28%B over 170 minutes with Buffer A comprising 3% acetonitrile, 0.4% FA and Buffer B comprising 100% acetonitrile, 0.4% FA. The column was packed with 1.8 μm C18 beads with a pore size of 12 nm (Sepax Technologies Inc.) heated to 60°C using a column heater (constructed in-house). Samples from the HPLC were injected into an Orbitrap Fusion Lumos Tribrid MS (ThermoFisher, Catalog Number FSN02–10000) using a multi-notch MS3 method[47,48]. MS scans were performed in the Orbitrap over a scan range of 400–1400 m/z with dynamic exclusion. The top 10 ions with charge states from 2 to 6 were selected for MS/MS. Rapid rate scans were performed in the Ion Trap with a collision energy of 35% and a maximum injection time of 120 ms. TMT quantification was performed using SPS-MS3 in the Orbitrap with a scan range of 100–1000 m/z and an HCD collision energy of 55%. Orbitrap resolution was 50,000 (dimensionless units) with a maximum injection time of 150 ms. MS isolation windows were varied depending on the charge state. Further details on LC and MS parameters and settings used were described recently[49].

Proteomics data analysis.—A compilation of commercially available software (Core software program) was used to convert mass spectrometric data (Thermo ".RAW" files) to mzXML format and to correct monoisotopic m/z measurements and erroneous peptide charge state assignments. Assignment of MS/MS spectra was performed using the Sequest[50] (version 28 (http://fields.scripps.edu/yates/wp/?page_id=17)) and the Human UniProt database (downloaded February 2014). The database search included reversed protein sequences and known contaminants such as human keratins which were excluded for subsequent analyses. Linear discriminant analysis was used to distinguish forward and reverse hits[51]. Peptides were identified using an MS2 spectrum and a false discovery rate (FDR) < 1% and was achieved by applying the target-decoy database search strategy. Filtering was performed as described previously[48]. Variable extents of modification including the presence of oxidized methionine and over-labelling of TMT on serine, threonine and tyrosine[52] were considered during peptide assignment for whole-protein experiments. For protein identification and quantification, shared peptides were collapsed into the minimally sufficient number of proteins using rules of parsimony. Peptides with a total TMT value of > 200 and an isolation specificity of > 0.7 were included for quantification.

Cell Viability assay.

For 72-h viability assays using growth rate inhibition method, cells were plated in 96-well plates at 6×10^3 cells/well for 24 hours. Subsequently, time 0 was measured before cells were treated with a test compound at doses ranging from 10 nM to 10 μM for 72 hours. Number of viable cells was determined using the CellTiter-Glo Luminescent Cell. Time 0 and Time 72h, dose range and corresponding luminescence intensity were uploaded to the GR_{50} calculator (http://www.grcalculator.org/grcalculator/) to generate GR values, GR_{50}

and GR_{max}. GraphPad Prism 8.0 (GraphPad Software Inc.) was used to plot dose response curves.

Fluorescence-activated cell sorting analysis (FACS).

For cell cycle analysis, cells (0.5×10^6) were treated with the test compounds at indicated concentrations for 24 h. The cells were dispensed with ice-cold 70% ethanol and subsequently fixed at $-20°C$, treated with RNase A (0.5 mg/ml) and stained with propidium iodide (PI) (50 μg/ml) until analysis. Samples were analyzed on a LSRFortessa™ cell analyzer (BD Biosciences) using BD FACSDiva. A minimum of 5×10^4 events were counted per samples for analysis. Data were analyzed using FlowJo software.

RT-PCR.

Total RNA was isolated with the RNAeasy Mini kit (QIAGEN). One μg of purified RNA was reverse transcribed using Superscript III First-Strand (Invitrogen) with random hexamer primers following the manufacturer's protocol. Quantitative PCR was carried out using the QuantiFast SYBR Green PCR kit (Qiagen) and analyzed on an Applied Biosystems StepOne Real-Time PCR System (Life Technologies). Each individual biological sample was qPCR-amplified in technical triplicate and normalized to GAPDH as an internal control. Relative quantification was calculated according to the Ct relative quantification method. Error bars indicate ± SD of three replicates. Primers sequences are available on request.

Poly(A) 3' processing and analysis was performed as in Krajewska et al. with some minor modifications and summarized below[52]. *Poly(A) 3′-end sequencing.* Jurkat cells were exposed to DMSO or THZ531 (250 nM) or to BSJ-4-116 or BSJ-4-116NC (50 nM) for 8 h. RNA extraction was performed with TRIzol (Ambion) following the manufacturers' instructions. Total RNA was treated with DNase I (Invitrogen). Sequencing libraries were prepared with the RNA-seq library kit (QuantSeq 3′ mRNA Sequencing REV, Lexogen) following the manufacturers' instructions. All samples were sequenced on a HiSeq 2500 sequencer.

Poly(A) 3′-sequencing data processing.—For each sample single-end 100 bp reads were obtained and filtered using bbduk.sh from BBMap (v37.00) and parameters "k = 13 ktrim = r useshortkmers = t mink = 5 qtrim = r trimq = 20 minlength = 75 ref = truseq_rna.fa.gz" to remove potential adapter contamination or low-quality reads. High-quality reads were subsequently mapped to the human genome (GRCh38) with STAR (version STAR_2.5.1b_modified) and the following para- meters "--outFilterType BySJout --outFilterMultimapNmax 20 --alignSJo- verhangMin 8 --alignSJDBoverhangMin 1 --outFilterMismatchNmax 999 --outFilterMismatchNoverLmax 0.1 --alignIntronMin 20 --alignIntronMax 1000000 --alignMatesGapMax 1000000 --outSAMattributes NH HI NM MD --outSAMtype BAM SortedByCoordinate". To create strand-specific sample cov- erage profiles in 50 bp bins, we used bamCoverage (DeepTools v2.5.4) with para- meters "-- normalizeUsingRPKM –filterRNAstrand –bs 50". Genome-wide correlation of biological replicates was calculated using Spearman's rank coefficient and visualized using scatterplots and heatmaps. These results showed high reproducibility for each condition and hence, for all visualizations, replicates were merged using samtools merge and processed again as

described for the individual replicates. ERCC spike-in sequences were added and used to compute sample specific size factors to allow the detection of absolute gene expression level differences.

Poly(A) 3′-sequencing peak identification and filtering.—Poly(A)-seq peaks were called using MACS2 (v 2.1.1) and parameters "--nomodel --extsize 100 --shift 0" using a merged bam file of all samples. To identify false positive poly(A) peaks, two criteria were used: (1) the presence of the potential PAS motifs (AATAAA, ATTAAA, AGTAAA, TATAAA, AATATA, AATACA, CATAAA, GATAAA, AATGAA, ACTAAA, AAGAAA, AATAGA) computed in a 100 bp window upstream of the peak in a strand-specific manner, and (2) the presence of a genomic 25-adenine (A) stretch with a maximum of 3 mismatches computed in a 50 bp window downstream of the peak in a strand-specific manner. Peaks were removed if they were not associated with a PAS motif but were associated with a genomic stretch of A's. Retained Poly(A)-seq peaks were annotated in a step-wise manner; first, peaks were considered to be associated with the 3′ UTR if they were within the vicinity of the transcription end site (TES, −200 to +600 bp), next, the remaining peaks were considered to be intergenic or genic and, in the latter case, overlapping with an exon or intron. If a peak overlapped multiple transcripts, priority was given to protein-coding transcripts followed by longer transcripts. For metagene plots genes were represented by the isoform that showed the highest combined 3′-UTR expression level.

Metagene profiles.—A gene metaprofile was created by dividing each gene (from TSS to TES) into 50 equally sized bins; 2 kb upstream and downstream flanking regions were binned in bins of 100 bp. Bedgraph files with normalized reads from TT-seq or poly(A) 3′-seq were used to calculate read density (RPM/bp) across those bins and subsequently summarized for all genes. To create a TSS or TES metaprofile, we followed an analogous approach with variable upstream and downstream flanking regions and summarized bins of 50 bp. To compare TT-seq and poly(A) 3′-seq profiles, calculated read densities were rescaled between 1 and 100.

Correlation of transcript length and 3′ expression changes.—To identify differential expressed genes based on 3′ poly(A)-sequencing, all counts for 3′ UTR-associated polyadenylation sites were summarized per gene. This data matrix was log2 normalized and used to identify differential expression and fold-changes with the limma package in R. Correlation between fold-changes and transcript length was performed on the highest expressed transcript for each gene in the control condition. A generalized additive model (GAM) smoothing curve was fitted to each treatment to observe global changes and for visualization purposes.

Intronic polyadenylation usage.—For each transcript (TPM > 1) the reads of all intronic and 3′ UTR-associated poly(A) sites were summarized. To compare the change and usage of intronic versus 3′ UTR-associated poly(A) sites between different treatments, an odds ratio (OR) was calculated for each treatment sample but excluding transcripts that had no intronic poly(A) sites in either treatment. A two-sample Kolmogorov-Smirnov test was then used to detect changes in OR distributions between different treatments.

Enrichment analysis.—Gene Set Enrichment Analysis (GSEA) for gene sets of biological processes (BP) was performed using the GSEA Preranked tool from the Broad institute.

Whole exome sequencing.

Both parental and resistant clones of Jurkat cells were sent to Novogene for whole exome sequencing with duplicates. Sequencing libraries were generated by Agilent sureselect human all exon V6 kit. 8.3G data was obtained for each sample on average with Q30 of 92.5%, Sequencing data was trimmed using cutadapt (https://cutadapt.readthedocs.io/en/stable/) with "-q 20, 20 -m 90 -trim-n" to remove adaptors and low-quality reads. BWA-mem (http://bio-bwa.sourceforge.net) was used to align the reads to human reference genome hg.19. Duplicating reads were marked by picard Markduplicates (https://broadinstitute.github.io/picard). GATK (https://gatk.broadinstitute.org/hc/en-us) was used to do indel realignment and subsequent mutations calls with mutect2. Variants were filtered by Filtermutectcalls with "max_events-in-region 5" and "false-discovery-rate 0.01". Other parameters used in GATK calls were default. Variant annotation was carried out using Annovar (https://doc-openbio.readthedocs.io/projects/annovar/en/latest/). Loss of function mutations such as frameshift and stop gain were removed. Nonsynonymous exonic point mutations were kept. Mutations with average read depth less than 10 or in genomic duplication region (i.e. genomicSuperDups > 95%) were also removed from further analysis. In addition, only mutations with allele frequency greater than 25% in resistant cells were kept.

In vitro CDK12 kinase assay.

Wild type CDK12 kinase assay.—This assay was performed by Reaction Biology Corporation according to standard methods with minor modifications to the reported protocol. Briefly, compounds were tested in 12-point dose response, at a maximum concentration of 10 μM. Assays were performed at an ATP concentration of 30 μM (Km) CDK12/cyclin K.

Mutated CDK12 kinase assay.—Recombinant GST-CDK12 (714–1063)/GST-Cyclin K (1–267) was co-expressed with Cdk-Activating Kinase (CAK) from S. cerevisiae in *Sf9* insect cells using the MultiBacTurbo system[53]. Site-directed mutagenesis was used to generate CDK12 point-mutations (I733V).

After expression for 72 hours, cells were harvested by centrifugation. Cells were resuspended in lysis buffer (50 mM Hepes pH 7.4, 300 mM NaCl, 5% glycerol and 5 mM bMe) and disrupted by sonication. After centrifugation in a Beckman Avanti J-26S XP with a JA-25.50 rotor (20,000 rpm for 45 min at 10°C), lysate was applied to GST Trap FF columns (GE Healthcare) equilibrated with Lysis buffer using an Äkta Prime chromatography system (GE Healthcare) followed by extensive washes with 10 column volumes (CV) of lysis buffer. Proteins were eluted in elution buffer (50 mM Hepes pH 7.4, 300 mM NaCl, 5% glycerol, 5 mM bMe and 10 mM Glutathione) and incubated over night with Tobacco etch virus protease for tag-cleavage. Size exclusion chromatography (SEC) on a Superdex 200 PG column (GE Healthcare) was used to further purify the complex

using SEC buffer (200 mM Hepes pH 7.4, 150 mM NaCl, 5% glycerol and 1 mM TCEP). Fractions of the main peak were analyzed by SDS–PAGE and stoichiometric kinase complex was pooled and concentrated using Amicon filters (Millipore). Proteins were aliquoted, snap frozen in liquid nitrogen and stored at −80°C.

Radioactive kinase activity measurements were performed using 0.2 mM [γ–^{32}P]-ATP containing 0.45 mCi ^{32}P/mL (Perkin Elmer). CDK12/CycK complexes were pre-incubated at 0.2 μM with varying concentrations of compound for 5 minutes at 30°C, followed by addition of substrate and an additional incubation for 15 minutes at 30°C. Reactions were stopped by EDTA, added to a final concentration of 50 mM. Mixtures were spotted onto filter sheets of Amersham Protran nitrocellulose membrane (GE Healthcare) and washed three times for 5 minutes with 0.75% (v/v) phosphoric acid. Radioactivity was counted in a Beckman Liquid Scintillation Counter (Beckman-Coulter) for 1 minute.

NanoBRET Ternary Complex Experiments.

MOLT-4 cells (ATCC) were grown and maintained in RPMI 1640 medium (Gibco) supplemented with 10% FBS (Seradigm) prior to performing experiments. 2×10^6 cells were electroporated with 2 μg total plasmid DNA per reaction consisting of one of each of the following CDK proteins: full-length human CDK12 (Uniprot Q9NYV4), CDK12 (I733V), CDK12 (G739S), CDK12 (K745R), CDK12 (L752M), CDK12 (K745R/L752M) or full-length CDK13 (Uniprot Q14004), CDK13 R723K, CDK13 M730L, CDK13 R723K/ M730L fused at the C-terminus with NanoLuc in combination with HaloTag-CRBN at a 1:10 donor (NanoLuc) to acceptor (HaloTag) DNA ratio. Reactions were assembled in 100 μL volume using the Amaxa Cell Line Nucleofector Kit L (Lonza) and were pulsed using the Nucleofector 2b Device (Lonza) and program C-005. Following electroporation, cells were incubated in growth medium in a 6-well plate for 24 hours at 37°C and 5% CO_2 before plating 3.5×10^5 cells/well into 96-well white assay plates in the presence and absence of HaloTag NanoBRET 618 ligand (Promega) and 30 nM BSJ-4-116 or BSJ-4-116 NC compounds. Following a 3-hour incubation at 37°C and 5% CO_2, NanoBRET NanoGlo substrate (Promega) was added to the plate, and dual filtered luminescence was collected using a CLARIOstar plate reader (BMG Labtech) equipped with a 460/80 nm bandpass filter and a 610 nm long pass filter (acceptor, HaloTag NanoBRET ligand) using an integration time of 0.5 s. Background subtracted NanoBRET ratios expressed in milliBRET units were calculated from the equation:

$$\text{mBRET ratio} = \left(\frac{acceptor\ channel}{donor\ channel} - \frac{acceptor\ channel\ (no\ ligand)}{donor\ channel\ (no\ ligand)} \right) 1000$$

Fold increase in BRET was calculated by normalizing mBRET ratios to the average mBRET ratios for negative control BSJ-4-116-NC.

Quantification and Statistical Analysis

Data are presented as the means ± SD of a minimum of 3 experiments except where indicated. Student's *t*-test (two-tailed, unpaired) was used to compare the means for two groups, while one-way ANOVA was used in comparisons with multiple groups. Analyses

were performed with GraphPad Prism 7.02 (GraphPad Software). $P < 0.05$ was considered significant. No data were excluded.

Data availability statement

Dataset of Exonic nonsynonymous variants excluding loss of function mutations in Jurkat resistant cells is available in Supplementary Dataset 1. KINOMEscan data is provided in Supplementary Dataset 2. Complete GSEA result is provided in Supplementary Dataset 3. Whole exome sequencing data of parental and resistant cell lines to BSJ-4-116 has been deposited to NCBI sequence read archive with BioProject ID PRJNA634900. Poly(A) 3′-sequencing data has been deposited to the NCBI GEO (accession number: GSE161650). Human UniProt database. Crystal Structure of Human Cereblon in Complex with DDB1 and Lenalidomide (Protein Data Bank (PDB) ID 4TZ4). Crystal Structures of the Human CDK12-CyclinK Complex (PDB IDs 5ACB, 6CKX and 6B3E). Crystal Structures of the Human CDK13-CyclinK Complex (PDB ID 5EFQ).
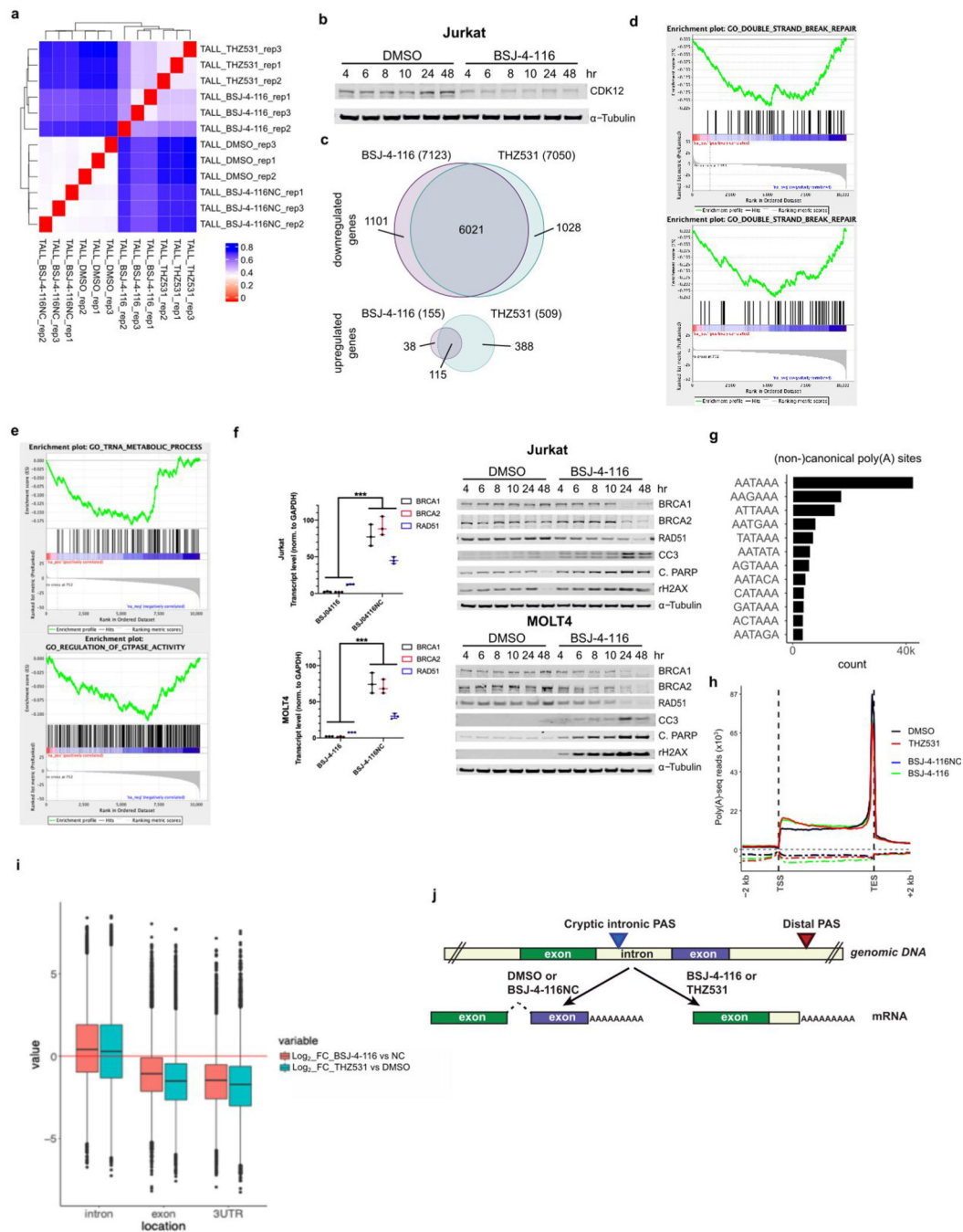
Extended Data
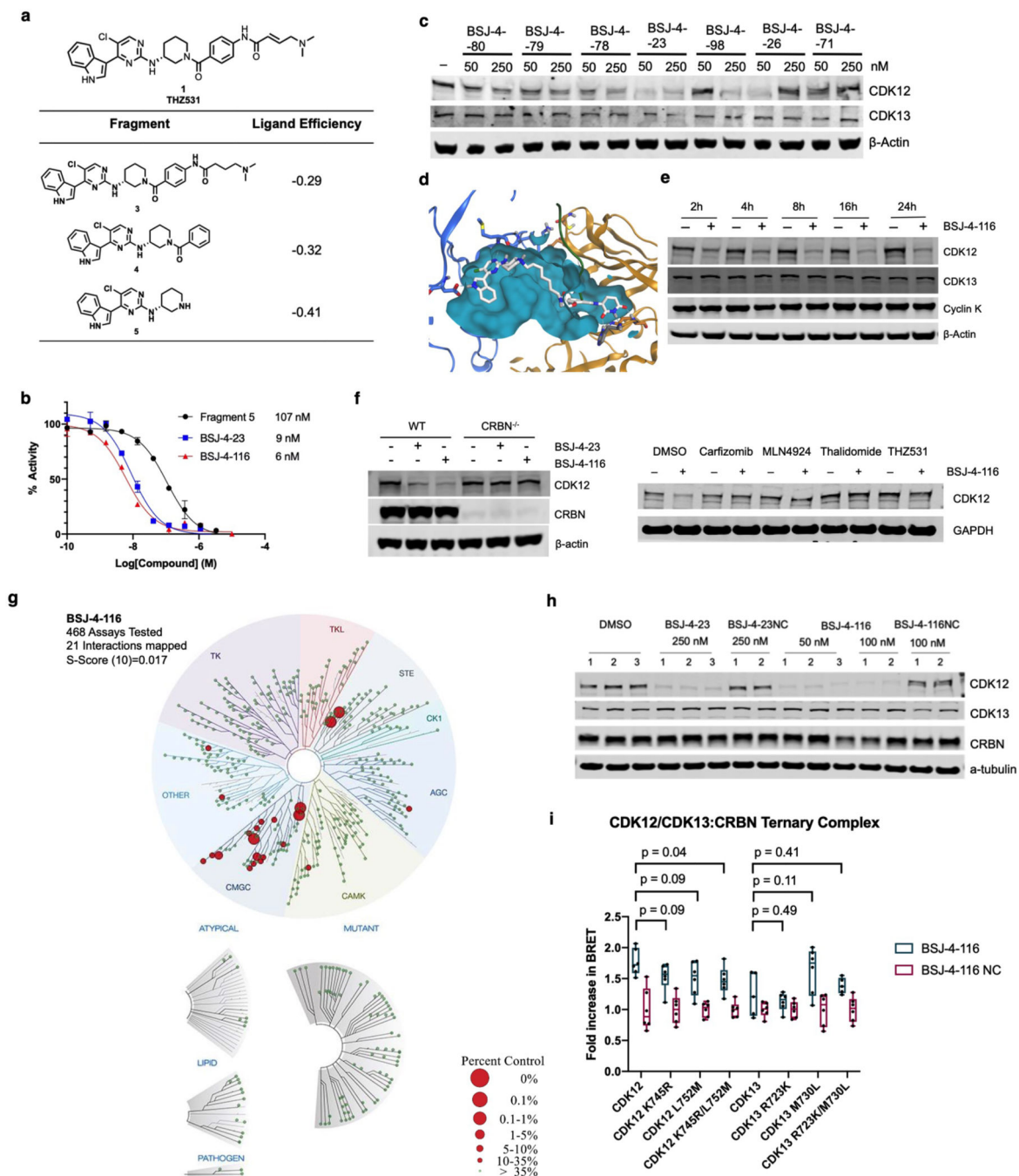
Extended Data Figure 1. Development of CDK12 degraders BSJ-4-23 and BSJ-4-116.
(**a**) Chemical structures of THZ531 and its 3 fragments with ligand efficiency values. (**b**) *In vitro* CDK12 kinase assay. Assays were performed at an ATP concentration of 30 μM (apparent Km). Data are presented as mean ± s.d. of *n* = 3 biologically independent samples. (**c**) Preliminary screening immunoblots for CDK12, CDK13 and β-Actin in Jurkat cells after 6 h treatment with DMSO or different CDK12 degraders at the indicated concentrations.

(**d**) Binding groove for BSJ-4-23 in modeled ternary complex of CDK12/BSJ-4-23/CRBN (CDK12 in blue, PDB ID: 5ACB, CRBN in orange, PDB ID: 4TZ4, BSJ-4-23 carbons in light grey). (**e**) Time-dependent effect of BSJ-4-116 (50 nM) on CDK12, CDK13 and cyclin K protein levels after 2 h, 4 h, 8 h, 16 h and 24 h treatment in Jurkat cells. (**f**) Left: Immunoblots for CDK12, CRBN and β-Actin in WT and CRBN null Jurkat cells after 6 h treatment with DMSO, BSJ-4-23 (250 nM) and BSJ-4-116 (50 nM); Right: Immunoblots for CDK12 and α-tubulin in Jurkat cells following 2 h pre-treatment with DMSO, Carfizomib (400 nM), MLN4924 (1000 nM), Thalidomide (1000 nM) and THZ531 (250 nM) followed by 6 h co-treatment with DMSO or BSJ-4-116 (50 nM). (**g**) KinomeScan kinase selectivity profile for BSJ-4-116. BSJ-4-116 was profiled at a concentration of 1 μM against a panel of 468 human kinases. The results for the binding interactions are reported as a percent of the DMSO control (% control), where larger red circles indicate stronger binding hits. The selectivity score was defined as the ratio of the number of kinases inhibited to a specified percentage versus the total number of kinases. (**h**) Degradation effect of BSJ-4-116 and BSJ-4-116NC at indicated doses prechecked by western blots for the proteomics experiment in Jurkat cells. (**i**) NanoBRET live cell ternary complex assays performed in MOLT-4 cells co-expressing HaloTag-CRBN and one of the following C-terminal NanoLuc fusions: CDK12, CDK12 (K745R), CDK12 (L752M), CDK12 (K745R/L752M) or CDK13, CDK13 (R723K), CDK13 (M730L), CDK13 (R723K/M730L). The fold increase in NanoBRET signal relative to BSJ-4-116NC was plotted after 3 h treatment with the indicated compounds with n=6 biologically independent samples.

Extended Data Figure 2. CDK12 degradation preferentially leads to premature cleavage and polyadenylation (PCPA) of long genes enriched with DDR genes.

(a) Genome-wide correlation analysis for replicates from each condition showing significant correlation between BSJ-4-116 vs THZ531, and DMSO vs BSJ-4-116NC. (b) Immunoblots for CDK12 and α-tubulin in Jurkat cells treated with DMSO or BSJ-4-116 (50 nM) for indicated hours. (c) Fisher exact test showing significant overlap in genes downregulated by BSJ-4-116 vs THZ531 (p=0). There was also significant overlap in the small numbers of gene upregulated (p=1.42e-136). (d) GSEA of downregulated genes in Jurkat cells treated with BSJ-4-116 and THZ531. (e) Additional enriched GSEA signatures enriched

by BSJ-4-116 treatment. (f) Left: qRT-PCR analysis of the indicated DDR gene expression in Jurkat and MOLT4 cells treated with BSJ-4-116 (50 nM) or BSJ-4-116NC (100 nM) for 10 h. Data were normalized to GAPDH and compared to DMSO-treated controls (n=3). Right: Immunoblots for indicated DDR and cell death markers in Jurkat and MOLT4 cells treated with DMSO or BSJ-4-116 (50 nM) for indicated hours. (g) Bar plot showing the frequency of retrieved polyadenylation site (PAS) motifs 100bp upstream of the poly(A) 3'-seq peaks. (h) Average metagene profiles of normalized poly(A) 3'-seq reads over gene bodies and extending –2 to +2 kb of all detected genes in Jurkat cells treated with BSJ-4-116 (50 nM) or THZ531 (250 nM) vs DMSO for 8 h. Sense and antisense reads are depicted by solid and dashed lines, respectively. (i) Boxplots showing the differential usage (log2 fold-change) of polyadenylation sites at three different genomic locations. The comparison BSJ-4-116 vs. BSJ-4-116NC is shown in red and THZ531 vs. DMSO is shown in green. (j) Schematic illustration of PCPA caused by CDK12 inhibition or degradation. Data in (b) and (f) are representative of n=2 independent experiments.
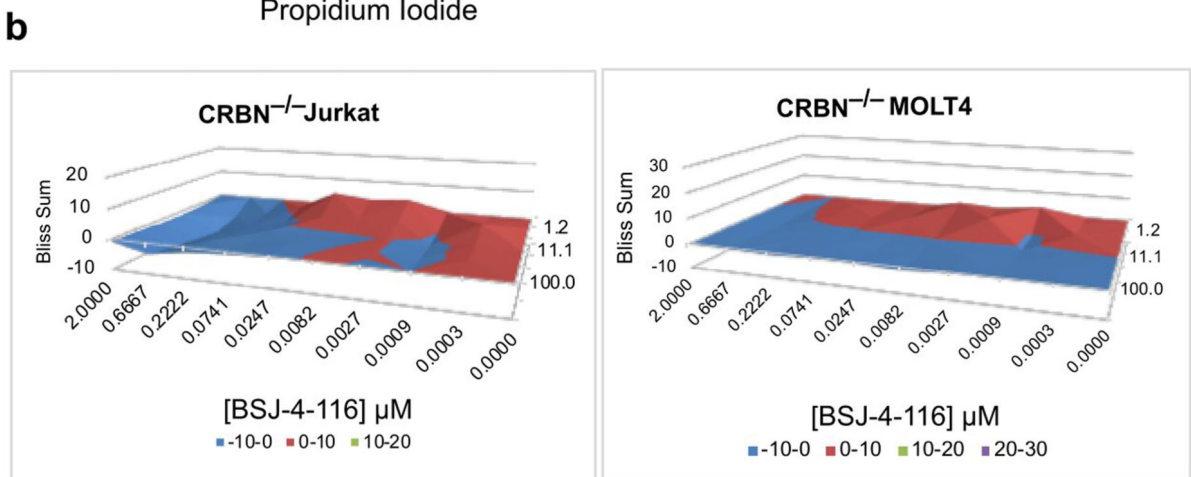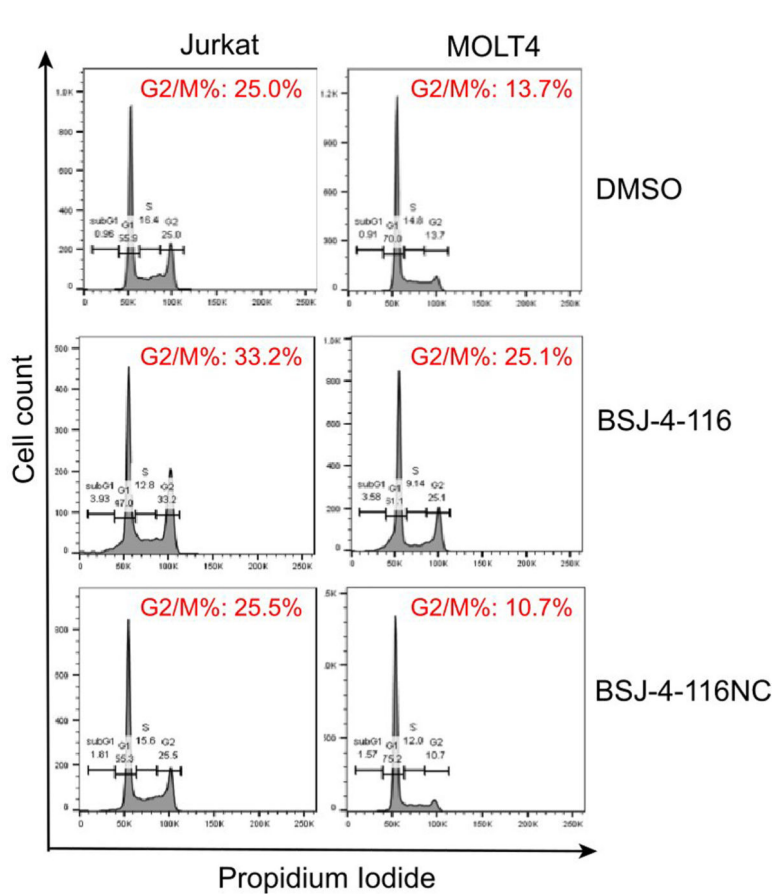
Extended Data Figure 3. BSJ-4-116 inhibits the growth of T-ALL cells and sensitizes them to PARP inhibition.

(**a**) Cell-cycle analysis of Jurkat and MOLT4 cells treated with BSJ-4-116 (50 nM) and BSJ-4-116NC (100 nM) for 24 h. DNA was stained with propidium iodide (PI) before flow cytometry analysis. G/M% values are presented as mean ± s.d. of n=2 biologically independent samples and are representative of n=2 independent experiments. (**b**) Excess over Bliss synergy plots for serial dilutions of BSJ-4-116 in combination with Olaparib in CRBN null Jurkat (top) and MOLT4 (bottom) cells. (n=3).
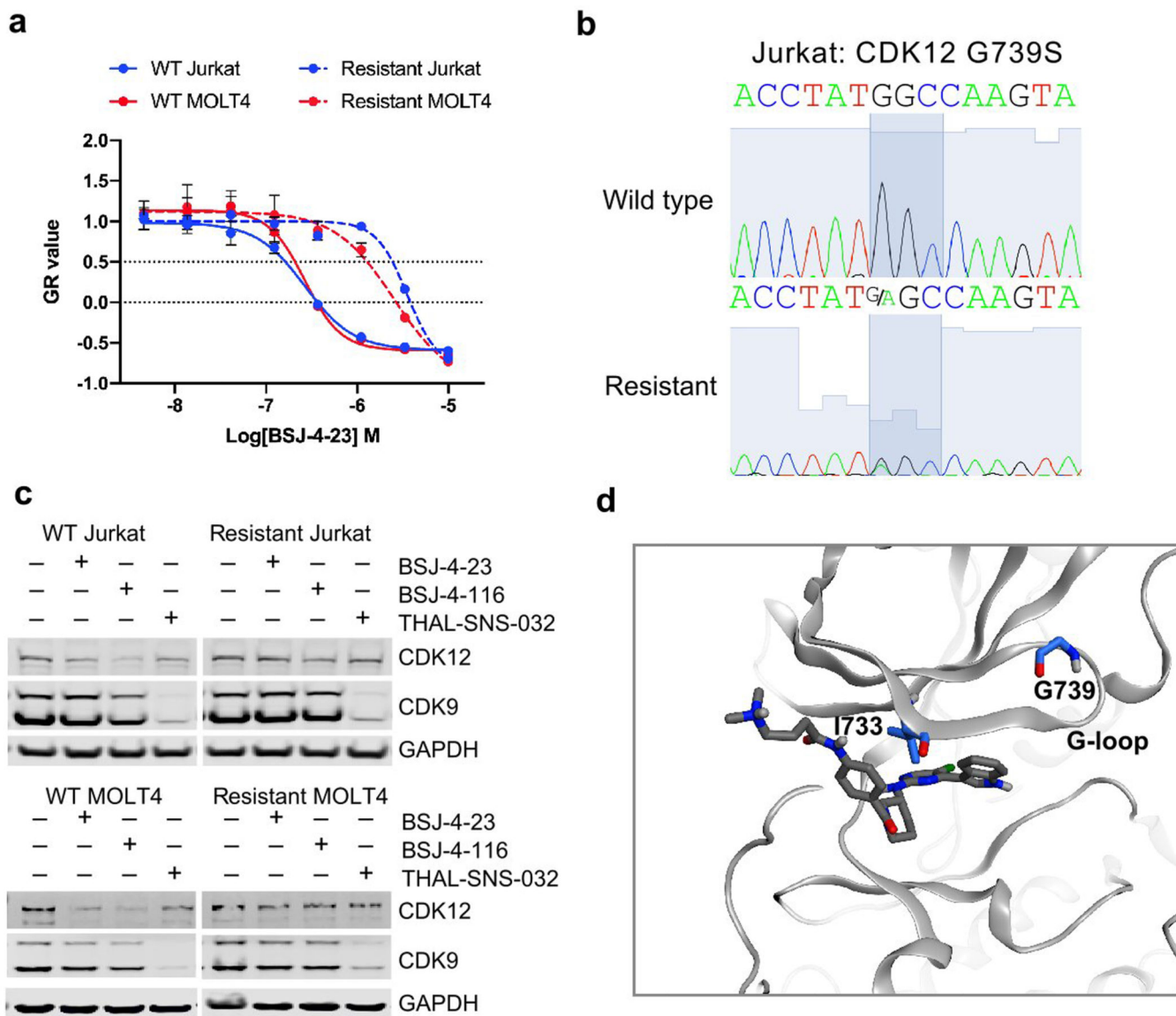
Extended Data Figure 4. Chronic exposure leads to acquired resistance to BSJ-4-116 mediated by G-loop mutations.

(**a**) Dose response curves for parental and resistant Jurkat and MOLT4 cells treated with BSJ-4-23 at indicated dose range for 72 h. Percent cell growth relative to DMSO-treated was analyzed using growth rate inhibition assay method. Data are presented as mean ± s.d. of n=3 biologically independent samples. (**b**) Detection of heterozygous G739S mutation in Jurkat resistant cells. DNA chromatograms of sanger sequencing shows region of mutation from PCR-amplified CDK12 cDNA. (**c**) Immunoblots for CDK12, CDK9 and GAPDH in parental and resistant Jurkat and MOLT4 cells treated with DMSO, BSJ-4-23 (250 nM), BSJ-4-116 (50 nM) or THAL-SNS-032 (250 nM) for 8 h. Data represent n=2 independent experiments. (**d**) CDK12 kinase domain structure (PDB code: 5ACB) showing the locations of G-loop mutations I733 and G739

Supplementary Material

Refer to Web version on PubMed Central for supplementary material.

Acknowledgements

Competing Financial Interests Statement

N.S.G. is a founder, science advisory board member (SAB) and equity holder in Gatekeeper, Syros, Petra, C4, B2S, Aduro and Soltego. The Gray lab receives or has received research funding from Novartis, Takeda, Astellas, Taiho, Janssen, Kinogen, Voronoi, Her2llc, Deerfield. Ephiphanes and Sanofi. J.C. is a consultant to Soltego, Jengu, Allorion, and equity holder for Soltego, Allorion, M3 bioinformatics & technology Inc. P.K.S. is a member of the SAB or Board of Directors of Merrimack Pharmaceutical, Glencoe Software, Applied Biomath and RareCyte Inc. and has equity in these companies. B.J., J.C., Y.G., N. K., T.Z., and N.S.G. are inventors on CDK12 degrader patents.

REFERENCES

1. Hydbring P, Malumbres M & Sicinski P Non-canonical functions of cell cycle cyclins and cyclin-dependent kinases. Nat Rev Mol Cell Biol 17, 280–292, doi:10.1038/nrm.2016.27 (2016). [PubMed: 27033256]

2. Shiekhattar R et al. Cdk-activating kinase complex is a component of human transcription factor TFIIH. Nature 374, 283–287, doi:10.1038/374283a0 (1995). [PubMed: 7533895]

3. Fisher RP Secrets of a double agent: CDK7 in cell-cycle control and transcription. J Cell Sci 118, 5171–5180, doi:10.1242/jcs.02718 (2005). [PubMed: 16280550]

4. Galbraith MD, Bender H & Espinosa JM Therapeutic targeting of transcriptional cyclin-dependent kinases. Transcription 10, 118–136, doi:10.1080/21541264.2018.1539615 (2019). [PubMed: 30409083]

5. Gajduskova P et al. CDK11 is required for transcription of replication-dependent histone genes. Nat Struct Mol Biol, doi:10.1038/s41594-020-0406-8 (2020).

6. Ramanathan Y et al. Three RNA polymerase II carboxyl-terminal domain kinases display distinct substrate preferences. J Biol Chem 276, 10913–10920, doi:10.1074/jbc.M010975200 (2001). [PubMed: 11278802]

7. Davidson L, Muniz L & West S 3' end formation of pre-mRNA and phosphorylation of Ser2 on the RNA polymerase II CTD are reciprocally coupled in human cells. Genes Dev 28, 342–356, doi:10.1101/gad.231274.113 (2014). [PubMed: 24478330]

8. Bartkowiak B et al. CDK12 is a transcription elongation-associated CTD kinase, the metazoan ortholog of yeast Ctk1. Genes Dev 24, 2303–2316, doi:10.1101/gad.1968210 (2010). [PubMed: 20952539]

9. Blazek D et al. The Cyclin K/Cdk12 complex maintains genomic stability via regulation of expression of DNA damage response genes. Genes Dev 25, 2158–2172, doi:10.1101/gad.16962311 (2011). [PubMed: 22012619]

10. Li X, Chatterjee N, Spirohn K, Boutros M & Bohmann D Cdk12 Is A Gene-Selective RNA Polymerase II Kinase That Regulates a Subset of the Transcriptome, Including Nrf2 Target Genes. Sci Rep 6, 21455, doi:10.1038/srep21455 (2016). [PubMed: 26911346]

11. Iniguez AB et al. EWS/FLI Confers Tumor Cell Synthetic Lethality to CDK12 Inhibition in Ewing Sarcoma. Cancer Cell 33, 202–216 e206, doi:10.1016/j.ccell.2017.12.009 (2018). [PubMed: 29358035]

12. Dubbury SJ, Boutz PL & Sharp PA CDK12 regulates DNA repair genes by suppressing intronic polyadenylation. Nature 564, 141–145, doi:10.1038/s41586-018-0758-y (2018). [PubMed: 30487607]

13. Krajewska M et al. CDK12 loss in cancer cells affects DNA damage response genes through premature cleavage and polyadenylation. Nat Commun 10, 1757, doi:10.1038/s41467-019-09703-y (2019). [PubMed: 30988284]

14. Negrini S, Gorgoulis VG & Halazonetis TD Genomic instability--an evolving hallmark of cancer. Nat Rev Mol Cell Biol 11, 220–228, doi:10.1038/nrm2858 (2010). [PubMed: 20177397]

15. Lui GYL, Grandori C & Kemp CJ CDK12: an emerging therapeutic target for cancer. J Clin Pathol 71, 957–962, doi:10.1136/jclinpath-2018-205356 (2018). [PubMed: 30104286]

16. Bayles I et al. Ex vivo screen identifies CDK12 as a metastatic vulnerability in osteosarcoma. J Clin Invest 129, 4377–4392, doi:10.1172/JCI127718 (2019). [PubMed: 31498151]

17. Bradner JE, Hnisz D & Young RA Transcriptional Addiction in Cancer. Cell 168, 629–643, doi:10.1016/j.cell.2016.12.013 (2017). [PubMed: 28187285]

18. Paculova H et al. BRCA1 or CDK12 loss sensitizes cells to CHK1 inhibitors. Tumour Biol 39, 1010428317727479, doi:10.1177/1010428317727479 (2017).

19. Zhang T et al. Covalent targeting of remote cysteine residues to develop CDK12 and CDK13 inhibitors. Nat Chem Biol 12, 876–884, doi:10.1038/nchembio.2166 (2016). [PubMed: 27571479]

20. Gao Y et al. Overcoming Resistance to the THZ Series of Covalent Transcriptional CDK Inhibitors. Cell Chem Biol 25, 135–142 e135, doi:10.1016/j.chembiol.2017.11.007 (2018). [PubMed: 29276047]

21. Johannes JW et al. Structure-Based Design of Selective Noncovalent CDK12 Inhibitors. ChemMedChem 13, 231–235, doi:10.1002/cmdc.201700695 (2018). [PubMed: 29266803]

22. Ito M et al. Discovery of 3-Benzyl-1-(trans-4-((5-cyanopyridin-2-yl)amino)cyclohexyl)-1-arylurea Derivatives as Novel and Selective Cyclin-Dependent Kinase 12 (CDK12) Inhibitors. J Med Chem 61, 7710–7728, doi:10.1021/acs.jmedchem.8b00683 (2018). [PubMed: 30067358]

23. Quereda V et al. Therapeutic Targeting of CDK12/CDK13 in Triple-Negative Breast Cancer. Cancer Cell 36, 545–558 e547, doi:10.1016/j.ccell.2019.09.004 (2019). [PubMed: 31668947]

24. Fan Z et al. CDK13 cooperates with CDK12 to control global RNA polymerase II processivity. Science Advances 6, doi:10.1126/sciadv.aaz5041 (2020).

25. Liang K et al. Characterization of human cyclin-dependent kinase 12 (CDK12) and CDK13 complexes in C-terminal domain phosphorylation, gene transcription, and RNA processing. Mol Cell Biol 35, 928–938, doi:10.1128/MCB.01426-14 (2015). [PubMed: 25561469]

26. Greifenberg AK et al. Structural and Functional Analysis of the Cdk13/Cyclin K Complex. Cell Rep 14, 320–331, doi:10.1016/j.celrep.2015.12.025 (2016). [PubMed: 26748711]

27. Olson CM et al. Pharmacological perturbation of CDK9 using selective CDK9 inhibition or degradation. Nat Chem Biol 14, 163–170, doi:10.1038/nchembio.2538 (2018). [PubMed: 29251720]

28. Jiang B et al. Development of Dual and Selective Degraders of Cyclin-Dependent Kinases 4 and 6. Angew Chem Int Ed Engl 58, 6321–6326, doi:10.1002/anie.201901336 (2019). [PubMed: 30802347]

29. Brand M et al. Homolog-Selective Degradation as a Strategy to Probe the Function of CDK6 in AML. Cell Chem Biol 26, 300–306 e309, doi:10.1016/j.chembiol.2018.11.006 (2019). [PubMed: 30595531]

30. Salami J et al. Androgen receptor degradation by the proteolysis-targeting chimera ARCC-4 outperforms enzalutamide in cellular models of prostate cancer drug resistance. Commun Biol 1, 100, doi:10.1038/s42003-018-0105-8 (2018). [PubMed: 30271980]

31. Sun Y et al. Degradation of Bruton's tyrosine kinase mutants by PROTACs for potential treatment of ibrutinib-resistant non-Hodgkin lymphomas. Leukemia 33, 2105–2110, doi:10.1038/s41375-019-0440-x (2019). [PubMed: 30858551]

32. Dobrovolsky D et al. Bruton tyrosine kinase degradation as a therapeutic strategy for cancer. Blood 133, 952–961, doi:10.1182/blood-2018-07-862953 (2019). [PubMed: 30545835]

33. Cooper JM et al. Overcoming BET Inhibitor Resistance in Malignant Peripheral Nerve Sheath Tumors. Clin Cancer Res 25, 3404–3416, doi:10.1158/1078-0432.CCR-18-2437 (2019). [PubMed: 30796033]

34. Cheng M et al. Discovery of Potent and Selective Epidermal Growth Factor Receptor (EGFR) Bifunctional Small-Molecule Degraders. J Med Chem 63, 1216–1232, doi:10.1021/acs.jmedchem.9b01566 (2020). [PubMed: 31895569]

35. Burslem GM & Crews CM Small-Molecule Modulation of Protein Homeostasis. Chem Rev 117, 11269–11301, doi:10.1021/acs.chemrev.7b00077 (2017). [PubMed: 28777566]

36. Watt GF, Scott-Stevens P & Gaohua L Targeted protein degradation in vivo with Proteolysis Targeting Chimeras: Current status and future considerations. Drug Discov Today Technol 31, 69–80, doi:10.1016/j.ddtec.2019.02.005 (2019). [PubMed: 31200862]

37. Burslem GM & Crews CM Proteolysis-Targeting Chimeras as Therapeutics and Tools for Biological Discovery. Cell 181, 102–114, doi:10.1016/j.cell.2019.11.031 (2020). [PubMed: 31955850]

38. Huang HT et al. A Chemoproteomic Approach to Query the Degradable Kinome Using a Multi-kinase Degrader. Cell Chem Biol 25, 88–99 e86, doi:10.1016/j.chembiol.2017.10.005 (2018). [PubMed: 29129717]

39. Choi SH et al. CDK12 phosphorylates 4E-BP1 to enable mTORC1-dependent translation and mitotic genome stability. Genes Dev 33, 418–435, doi:10.1101/gad.322339.118 (2019). [PubMed: 30819820]

40. Hafner M, Niepel M, Chung M & Sorger PK Growth rate inhibition metrics correct for confounders in measuring sensitivity to cancer drugs. Nat Methods 13, 521–527, doi:10.1038/nmeth.3853 (2016). [PubMed: 27135972]

41. Bosken CA et al. The structure and substrate specificity of human Cdk12/Cyclin K. Nat Commun 5, 3505, doi:10.1038/ncomms4505 (2014). [PubMed: 24662513]

42. Hopkins AL, Groom CR & Alex A Ligand efficiency: a useful metric for lead selection. Drug Discov Today 9, 430–431, doi:10.1016/S1359-6446(04)03069-7 (2004). [PubMed: 15109945]

43. Chirackal Manavalan AP et al. CDK12 controls G1/S progression by regulating RNAPII processivity at core DNA replication genes. EMBO Rep 20, e47592, doi:10.15252/embr.201847592 (2019).

44. Zhang L, Riley-Gillis B, Vijay P & Shen Y Acquired Resistance to BET-PROTACs (Proteolysis-Targeting Chimeras) Caused by Genomic Alterations in Core Components of E3 Ligase Complexes. Mol Cancer Ther 18, 1302–1311, doi:10.1158/1535-7163.MCT-18-1129 (2019). [PubMed: 31064868]

METHODS ONLY REFERENCES

45. Song Y et al. A dynamic view of the proteomic landscape during differentiation of ReNcell VM cells, an immortalized human neural progenitor line. Sci Data 6, 190016, doi:10.1038/sdata.2019.16 (2019). [PubMed: 30778261]

46. Wessel D & Flügge UI A method for the quantitative recovery of protein in dilute solution in the presence of detergents and lipids. Analytical Biochemistry 138, 141–143, doi:10.1016/0003-2697(84)90782-6 (1984). [PubMed: 6731838]

47. Ting L, Rad R, Gygi SP & Haas W MS3 eliminates ratio distortion in isobaric multiplexed quantitative proteomics. Nat Methods 8, 937–940, doi:10.1038/nmeth.1714 (2011). [PubMed: 21963607]

48. McAlister GC et al. MultiNotch MS3 enables accurate, sensitive, and multiplexed detection of differential expression across cancer cell line proteomes. Anal Chem 86, 7150–7158, doi:10.1021/ac502040v (2014). [PubMed: 24927332]

49. Paulo JA et al. Quantitative mass spectrometry-based multiplexing compares the abundance of 5000 S. cerevisiae proteins across 10 carbon sources. J Proteomics 148, 85–93, doi:10.1016/j.jprot.2016.07.005 (2016). [PubMed: 27432472]

50. Eng JK, McCormack AL & Yates JR An approach to correlate tandem mass spectral data of peptides with amino acid sequences in a protein database. Journal of the American Society for Mass Spectrometry 5, 976–989, doi:10.1016/1044-0305(94)80016-2 (1994). [PubMed: 24226387]

51. Elias JE & Gygi SP Target-decoy search strategy for increased confidence in large-scale protein identifications by mass spectrometry. Nat Methods 4, 207–214, doi:10.1038/nmeth1019 (2007). [PubMed: 17327847]

52. Krajewska M et al. CDK12 loss in cancer cells affects DNA damage response genes through premature cleavage and polyadenylation. Nat Commun 10, 1757, doi:10.1038/s41467-019-09703-y (2019). [PubMed: 30988284]

53. Bieniossek C, Imasaki T, Takagi Y & Berger I MultiBac: expanding the research toolbox for multiprotein complexes. Trends Biochem Sci 37, 49–57, doi:10.1016/j.tibs.2011.10.005 (2012). [PubMed: 22154230]
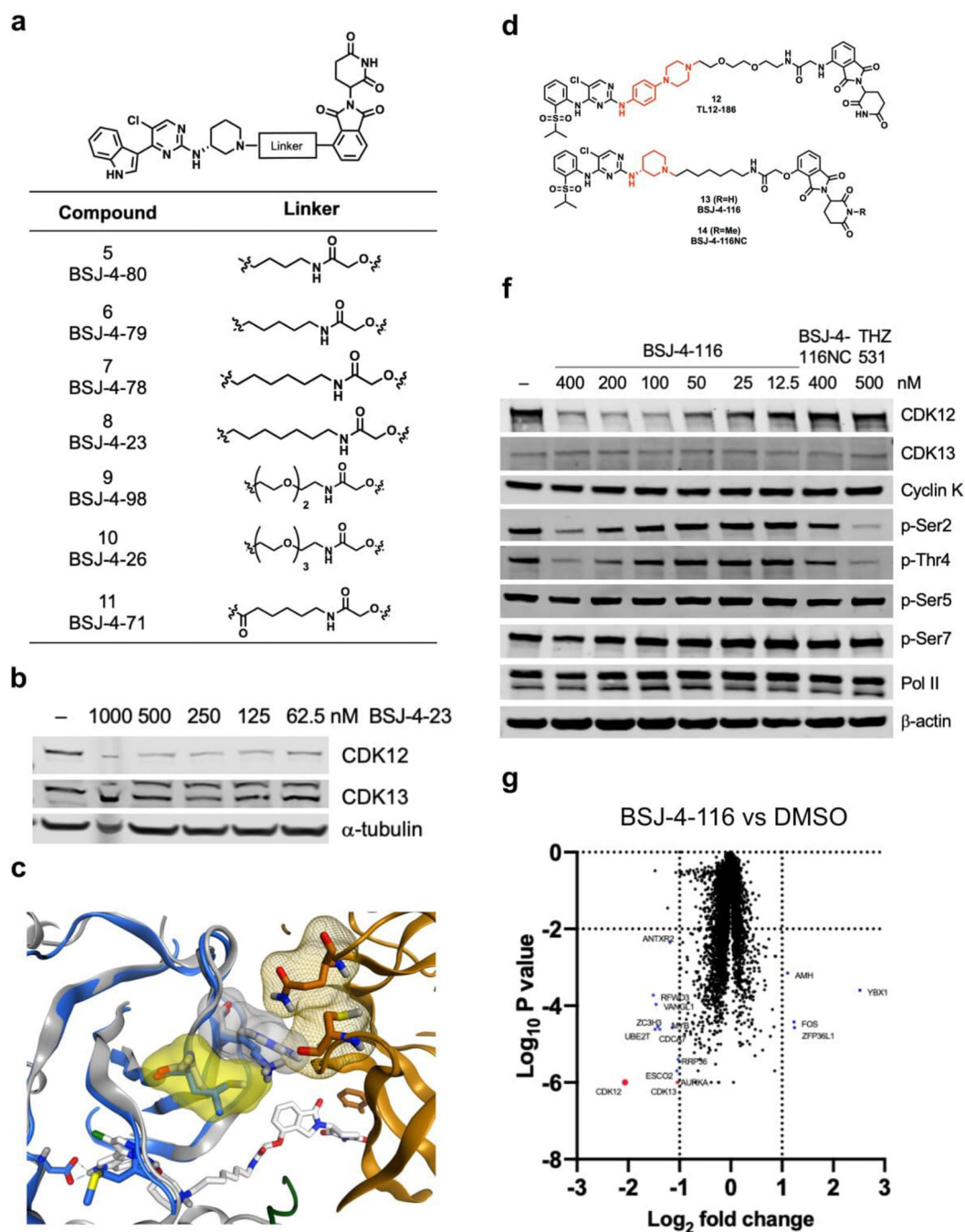
Figure 1. Development and characterization of CDK12 degrader BSJ-4-116.
(**a**) Chemical structures of CDK12 degraders derived from fragment 5 (Extended Data Figure 1). (**b**) Immunoblots for CDK12, CDK13 and α-tubulin in Jurkat cells after 6 h treatment with DMSO and BSJ-4-23 at indicated concentrations in nanomolar. Data represent n=2 independent experiments. (**c**) Superposition of CDK13 with modeled CDK12/BSJ-4-23/CRBN ternary complex (CDK12 in blue, PDB ID: 5ACB; CDK13 in grey, PDB ID: 5EFQ; BSJ-4-23 carbons in light grey; CRBN in orange, PDB ID: 4TZ4). The gray and yellow transparent surfaces are for R723 and M730 of CDK13, respectively. The

orange mesh is for CRBN Q325 and C394. (**d**) Chemical structures of a promiscuous kinase degrader TL12–186, a CDK12 degrader BSJ-4-116 (R=H) and its negative control BSJ-4-116NC (R=Me). (**e**) Immunoblots for CDK12, CDK13, Cyclin K, p-Ser2, p-Thr4, p-Ser5, p-Ser7, Pol II and β-actin in Jurkat cells after 6 h treatment with DMSO, BSJ-4-116, BSJ-4-116NC and THZ531 at the indicated concentrations. Data represent n=2 independent experiments. (**f**) Proteome-wide selectivity of BSJ-4-116. Quantitative proteomics showing relative abundance of proteins measure by multiplexed quantitative-mass spectrometry-based proteomics in Jurkat cells treated for 8 h with BSJ-4-116 (50 nM) or vehicle (DMSO). CDK12 and CDK13 are marked in red. Proteins marked in blue are a group of non-kinases affected by BSJ-4-116. Dotted lines indicate the threshold for statistically significantly degraded proteins (Log_{10} (p value) <-2 and Log_2 (fold change) <-1). Data are from n = 3 biologically independent samples.
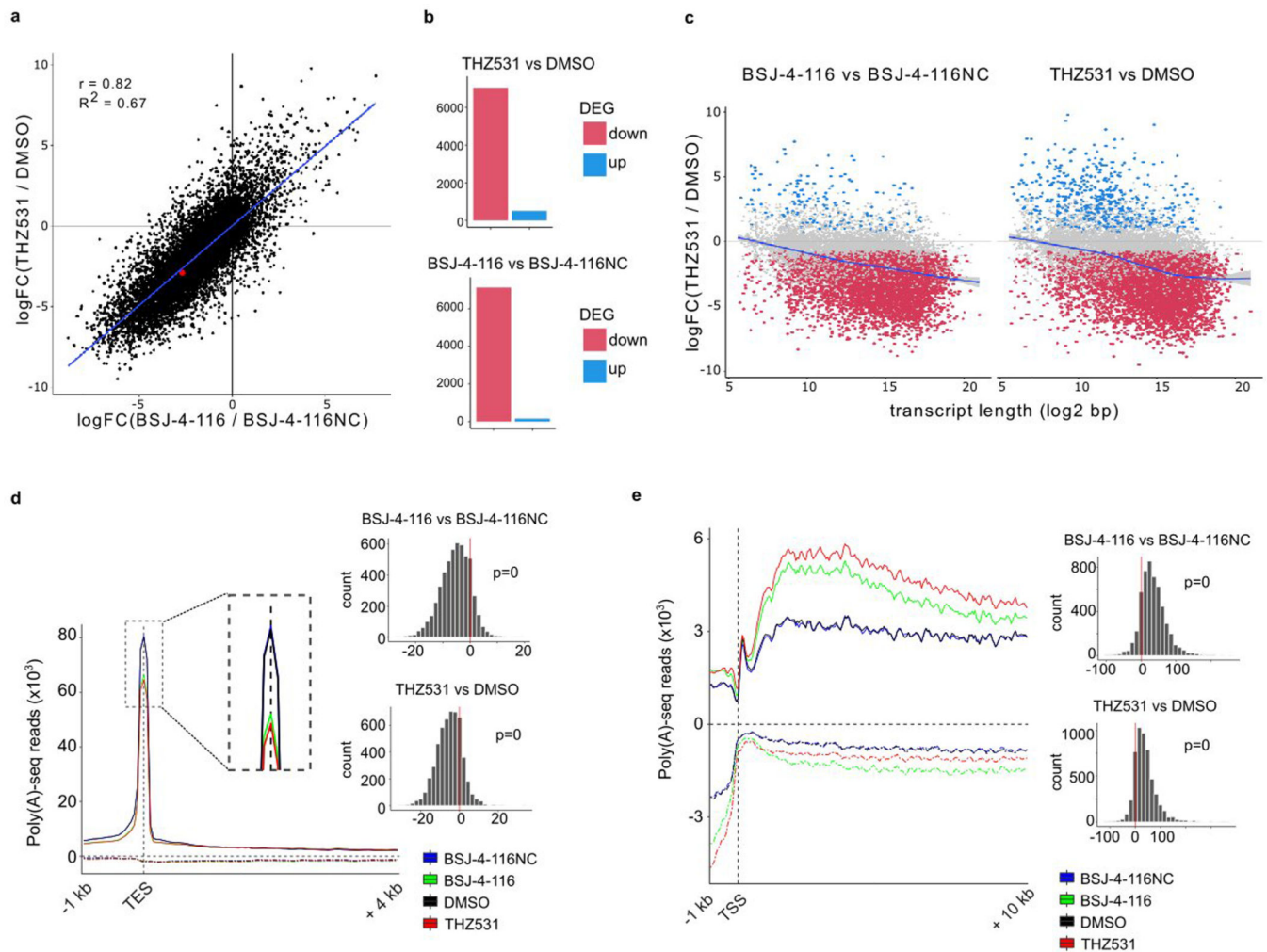
Figure 2. CDK12 degradation preferentially leads to premature cleavage and polyadenylation (PCPA) of long genes enriched with DDR genes.
(**a**) Scatter plot showing log2 fold-changes in gene expression in Jurkat cells treated with BSJ-4-116 (50 nM) vs. THZ531 (250 nM) for 8 h. BSJ-4-116 and THZ531 datasets were normalized to BSJ-4-116NC and DMSO, respectively. Red dot indicated CDK12. (**b**) Quantification of significantly up- and down-regulated genes in conditions illustrated in panel (**a**). (**c**) Scatter plot showing log2 fold-changes in gene expression vs gene length in log2 scale for each protein coding gene in cells treated as in panel (**a**). (**d**) Left panel, average metagene profiles of normalized poly(A) 3'-seq reads at the TES (–1 to +4 kb) for all detected in cells treated as in panel (**a**). Right panel, Wilcoxon test showing significant shift in reads towards in BSJ-4-116- and THZ531-treated (p=0). (**e**) Left panel, average metagene profiles of normalized poly(A) 3'-seq reads at the TSS (–1 to +10 kb) for all detected in cells treated as in panel (**a**). Right panel, Wilcoxon test showing significant shift in reads distribution towards positive in BSJ-4-116- and THZ531-treated (p=0).
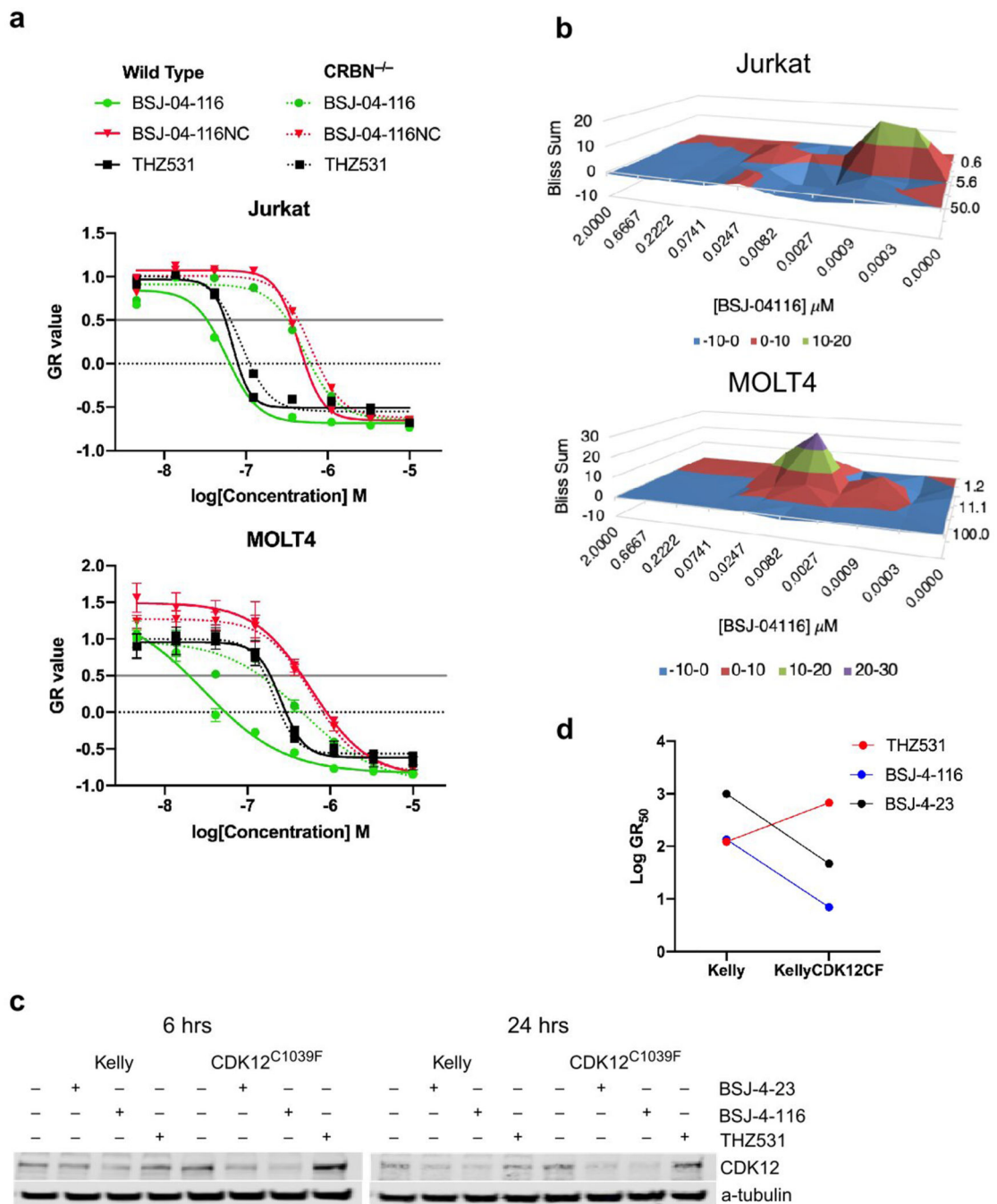
Figure 3. BSJ-4-116 inhibits the growth of T-ALL cells and sensitizes them to PARP inhibition.
(**a**) Dose response curves for wild type and CRBN null Jurkat (top) and wild type and
CRBN null MOLT4 (bottom) cells treated with BSJ-4-116, BSJ-4-116NC or thz531 at
indicated dose range for 72 h. Percent cell growth relative to DMSO-treated was analyzed
using growth rate inhibition assay method (see Methods and Materials for details). Data are
presented as mean ± s.d. of n=3 biologically independent samples and are representative
of n=2 independent experiments. (**b**) Excess over Bliss synergy plots for serial dilutions of
BSJ-4-116 in combination with Olaparib in Jurkat (top) and MOLT4 (bottom) cells. Excess

of Bliss score sum >0 indicates synergistic interaction. n=3 replicates. (**c**) Immunoblots for CDK12 and GAPDH in parental and $CDK12^{C1039F}$ (KellyCDK12CF) expressing Kelly cells treated with DMSO or BSJ-4-23 (250 nM) or BSJ-4-116 (50 nM) for 6 h and 24 h. Data are representative of n=2 independent experiments. (**d**) Dot plot depicting relative antiproliferative activity of BSJ-4-116, BSJ-4-23 and THZ531 in parental Kelly and KellyCDK12CF cells. GR_{50} values were obtained using the same protocol as in (**a**).
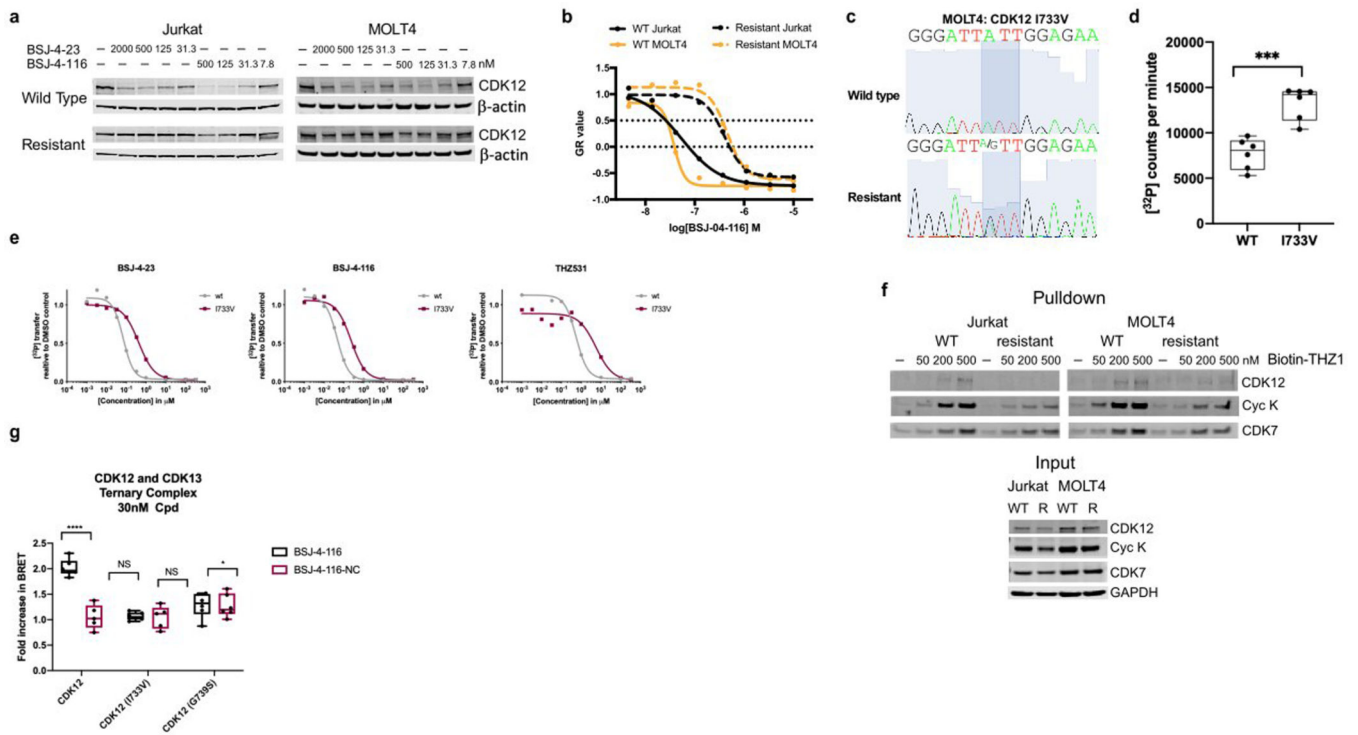
Figure 4. Chronic exposure leads to acquired resistance to BSJ-4-116 mediated by G-loop mutations.

(**a**) Immunoblots for CDK12 and GPADH in parental and resistant Jurkat and MOLT4 cells treated with BSJ-4-116 and BSJ-4-23 at indicated concentrations for 6 h. Data represent n=2 independent experiments. (**b**) Dose response curves for parental and resistant Jurkat and MOLT4 cells treated with BSJ-4-116 at indicated dose range for 72 h. Data are presented as mean ± s.d. of n=3 biologically independent samples and are representative of n=2 independent experiments. (**c**) Detection of heterozygous I733V mutation in MOLT4 resistant cells. DNA chromatograms of sanger sequencing shows region of mutation from PCR-amplified CDK12 cDNA.
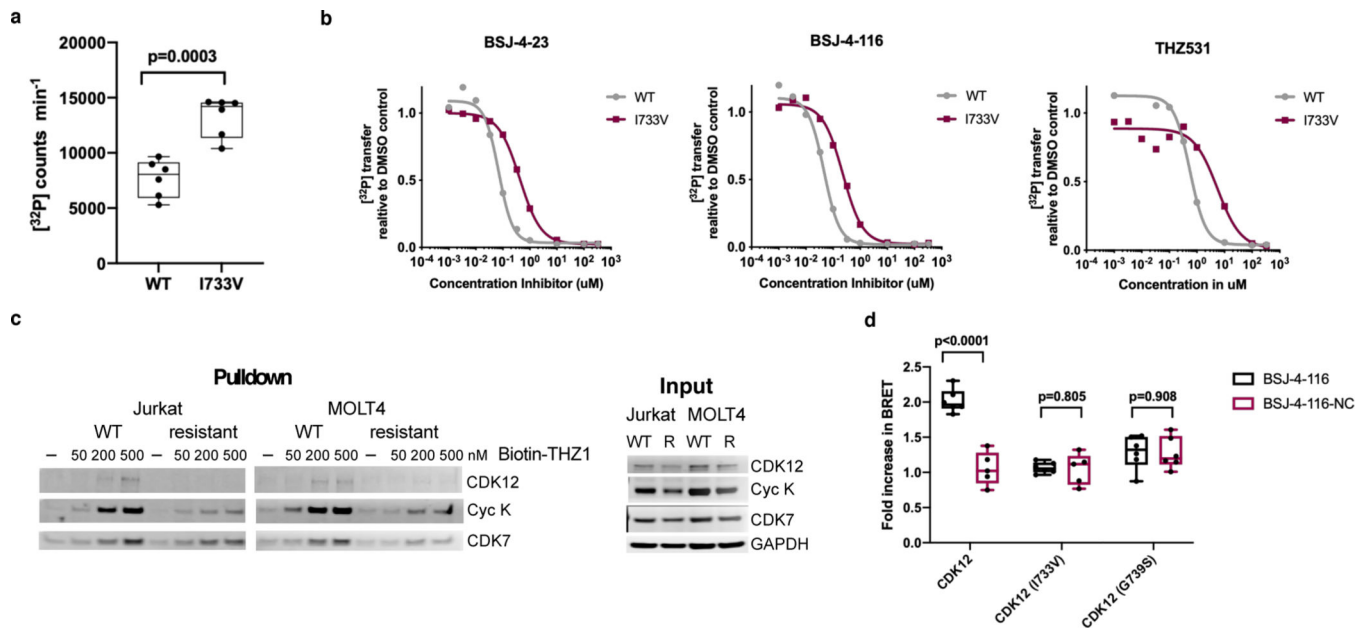
Figure 5. Chronic exposure leads to acquired resistance to BSJ-4-116 mediated by G-loop mutations.

(**a**) (**b**) ^{32}P-labeled ATP CDK12$^{WT/Mut}$ kinase assay. CDK12^{I733V} displayed increased kinase activity (**a**) and were less efficiently targetable with all compounds tested compared to wild type CDK12 (**b**). (**c**) Pulldown assays for CDK12 or cyclin K (Cyc K) and CDK7 with Biotin-THZ1 at indicated doses from parental or resistant Jurkat and MOLT4 cells. Immunoblots showing the relative capacity of THZ1 to enrich CDK12 (or Cyc K as a common surrogate) and CDK7 in parental and resistant cells. 25 μg total protein was loaded as controls for basal expression of CDK12, Cyc K, CDK7 and GAPDH expression. Data represent n=2 independent experiments. (**d**) NanoBRET live cell ternary complex assays performed in MOLT-4 cells co-expressing HaloTag-CRBN and one of the following C-terminal NanoLuc fusions: CDK12, CDK12 (I733V) or CDK12 (G739S). The fold increase in NanoBRET signal relative to BSJ-4-116NC was plotted after 3hr treatment with the indicated compounds. Data in (**a**), (**b**) and (**d**) are presented as mean ± s.d. of n=6 biologically independent samples and are representative of n=2 independent experiments.